



# Unveiling the synergy of polymorph heterointerface and sulfur vacancy in NiS/Ni<sub>3</sub>S<sub>2</sub> electrocatalyst to promote alkaline hydrogen evolution reaction

Kai Zhang<sup>a,b</sup>, Yuanxiao Duan<sup>a</sup>, Nigel Graham<sup>c</sup>, Wenzheng Yu<sup>a,\*</sup>

<sup>a</sup> State Key Laboratory of Environmental Aquatic Chemistry, Research Center for Eco-Environmental Sciences, Chinese Academy of Sciences, Beijing 100085, China

<sup>b</sup> State Key Laboratory of Urban Water Resource and Environment, Harbin Institute of Technology, Harbin 150090, China

<sup>c</sup> Department of Civil and Environmental Engineering, Imperial College London, South Kensington Campus, London SW7 2AZ, UK

## ARTICLE INFO

### Keywords:

Nickel sulfides  
Polymorph heterostructure  
Sulfur vacancy  
Alkaline hydrogen evolution  
Electrocatalysis

## ABSTRACT

Efficient transition metal sulfide electrocatalysts for alkaline hydrogen evolution reaction (HER) are desired but restricted by their sluggish kinetics. Herein, we report a hydrothermal sulfurization-acid assisted etching strategy for the controllable fabrication of Mo doped NiS/Ni<sub>3</sub>S<sub>2</sub> polymorph heterostructure with rich sulfur vacancies (Mo-NiS/Ni<sub>3</sub>S<sub>2</sub>-rich S<sub>v</sub>). Direct spectroscopic evidence, together with theoretical analysis, demonstrate that the S centers on the Ni<sub>3</sub>S<sub>2</sub> side of the nickel sulfide polymorphs are identified as the H<sub>2</sub>-evolving sites, while the Ni sites on the Mo-NiS side are beneficial for cleaving the HO-H bond. Importantly, in situ Raman spectroscopy further reveals that the presence of rich S<sub>v</sub> can expedite the evolution of H<sup>+</sup> to molecular H<sub>2</sub>, promoting the HER kinetics. As expected, the optimal Mo-NiS/Ni<sub>3</sub>S<sub>2</sub>-rich S<sub>v</sub> electrocatalyst exhibits the outstanding HER activity and excellent durability in alkaline solution. Understanding the synergy of polymorph heterostructure and element defect is crucial for the rational design of high-performance HER electrocatalysts.

## 1. Introduction

The hydrogen evolution reaction (HER) of alkaline water electrolysis, driven by renewable electricity, has been regarded as the most green and appealing approach for sustainable hydrogen production [1, 2]. The alkaline HER process involves two successive reaction steps: i) the formation of adsorbed H atoms (H<sub>ads</sub>) via electron-coupled water dissociation (Volmer step: H<sub>2</sub>O + e<sup>-</sup> → H<sub>ads</sub> + OH<sup>-</sup>); ii) the combination of H<sub>ads</sub> with another proton or adsorbed H to evolve molecular H<sub>2</sub> (Heyrovsky step: H<sub>ads</sub> + H<sub>2</sub>O + e<sup>-</sup> → H<sub>2</sub> + OH<sup>-</sup> or Tafel step: H<sub>ads</sub> + H<sub>ads</sub> → H<sub>2</sub>) [3,4]. The water dissociation step is highly energy demanding, resulting in high overpotentials required to perform efficient HER, and is commonly considered the rate determining step (RDS) [5,6]. As a typical example, state-of-the-art Pt catalysts exhibit about 2 or 3 orders of magnitude lower activity in alkaline media, than that in acidic media, due to the low efficiency of water dissociation [7]. On the other hand, the desorption of H<sub>ads</sub> intermediates to give H<sub>2</sub> plays a dominant role in determining the kinetics of the whole HER process [8,9]. The rational design of an advanced electrocatalyst to boost water dissociation and optimize the hydrogen binding energy is thus essential for enhancing alkaline HER activity.

To date, several strategies, including interface engineering and

vacancy creation, have been attempted to overcome the intrinsic activity limitation. Heterointerface engineering can modulate electronic properties and geometric structures, as well as chemisorption behavior, which directly influences the reactivity of reactants on catalysts [10,11]. More importantly, the heterointerface ensemble effect can integrate the active centers of different components to form multi-site reaction pathways for promoting the cleavage of HO-H bonds and accelerating the Volmer step [12]. Wang and co-workers constructed Pt<sub>3</sub>Ni/NiS interface nanowires to enhance the alkaline HER activity and stability, in which NiS was responsible for facilitating water dissociation, while Pt<sub>3</sub>Ni was considered to be the H<sub>2</sub>-evolving centers [13]. Nevertheless, considering the complexity and uncertainty of forming the desired heterointerfaces between these components, selected with appropriate compatibility and crystal structure, constructing the heterostructures between different polymorphs, such as Ni<sub>2</sub>P/NiP<sub>2</sub> [14], CoP/Co<sub>2</sub>P [15], B-Fe<sub>7</sub>S<sub>8</sub>/FeS<sub>2</sub> [16] and NiSe<sub>2</sub>/Ni<sub>3</sub>Se<sub>4</sub> [17], is becoming a promising route towards creating efficient electrocatalysts for alkaline HER. The polymorphs possess the compositional advantages, but feature diverse structural motifs, which makes them relatively easier to build the heterointerfaces. Very recently, Wang and co-workers demonstrated the water-induced formation of Ni<sub>2</sub>P/Ni<sub>12</sub>P<sub>5</sub> polymorphs by one-step phosphorization of nickel foam, which shows an enhanced alkaline

\* Corresponding author.

E-mail address: [wzyu@rcees.ac.cn](mailto:wzyu@rcees.ac.cn) (W. Yu).

<https://doi.org/10.1016/j.apcatb.2022.122144>

Received 31 July 2022; Received in revised form 1 November 2022; Accepted 3 November 2022

Available online 12 November 2022

0926-3373/© 2022 Elsevier B.V. All rights reserved.

HER performance [18]. Similarly, a self-standing MoC/Mo<sub>2</sub>C heterojunction electrode was fabricated via a one-step electro-carbiding approach to heighten the HER activity and durability in alkaline solution [19]. The interfaces of MoC-Mo<sub>2</sub>C polymorphs could modulate the interface Mo d orbital, which would significantly lower the energy barrier of water dissociation. In addition, it has been reported that vacancy engineering can modulate the electronic structure, surface properties and conductivity of the electrocatalysts [20]. For instance, the introduction of sulfur vacancies (S<sub>v</sub>) into metal sulfides presented a significant influence on the local environment around the active sites, which can optimize the adsorption behavior of the H intermediates and lower the kinetic energy gap of H<sub>ads</sub> converting to H<sub>2</sub>, thereby improving the HER activity [21].

In past decades, heazlewoodite-type Ni<sub>3</sub>S<sub>2</sub> with a stable trigonal structure has been studied extensively as HER electrocatalysts due to their suitable d-electron configuration, high conductivity and rich Ni-S bonds (Fig. S1) [22,23]. Previous research has demonstrated that the Ni<sub>3</sub>S<sub>2</sub> electrocatalyst requires a high energy to cleave the HO-H to form a strong S-H<sub>ads</sub> bond (363 KJ mol<sup>-1</sup>) during the alkaline HER process, resulting in the poor evolution of H<sub>ad</sub>\* to H<sub>2</sub> and low HER activity [24]. Fortunately, it has been reported that the NiS can serve as the water dissociation promoter and the S vacancies (S<sub>v</sub>) optimize the hydrogen adsorption free energy (ΔG<sub>H\*</sub>) [25,26]. In this case, incorporating NiS and S<sub>v</sub> into the Ni<sub>3</sub>S<sub>2</sub> system to construct polymorph heterointerfaces and defects would be an effective method to overcome the aforesaid dilemma but in great need of research.

Herein, we describe a novel, facile, acid-assisted strategy to introduce the S<sub>v</sub> into the NiS/Ni<sub>3</sub>S<sub>2</sub> polymorph heterostructure, prepared via hydrothermally sulfurizing the NiMoO<sub>4</sub> precursor. Characterization results revealed that the structural transformation between NiS and Ni<sub>3</sub>S<sub>2</sub> can be regulated by regulation of additive (sulfion and molybdenum) amount, inducing the optimized NiS/Ni<sub>3</sub>S<sub>2</sub> polymorph heterostructure. The Mo atom possesses the valence state diversity, endowing it good capability of regulating the electronic structures and the adsorption property of the nickel sulfides. The application of in-situ Raman spectroscopy verified that the S sites on the Ni<sub>3</sub>S<sub>2</sub> of the nickel sulfide polymorphs, were considered to be the H<sub>2</sub>-evolving centers and the presence of S<sub>v</sub> could accelerate the evolution of H\* to H<sub>2</sub>, thereby boosting the HER kinetics. Further theoretical calculation showed that the Ni centers of Mo-NiS were the water association promoter, which favored hydrogen transfer across the heterointerface to neighboring S sites of Ni<sub>3</sub>S<sub>2</sub>, and the S<sub>v</sub> could weaken the binding strength of S-H, facilitating the H desorption. As a result, the desired electrocatalyst exhibits excellent performance for alkaline HER and only needed 230 mV at 100 mA cm<sup>-2</sup>.

## 2. Experimental section

### 2.1. Reagents and materials

Nickel nitrate hexahydrate (Ni(NO<sub>3</sub>)<sub>2</sub>·6 H<sub>2</sub>O, Sinopharm Chemical Reagent, ≥ 98%), ammonium molybdate tetrahydrate ((NH<sub>4</sub>)<sub>6</sub>Mo<sub>7</sub>O<sub>24</sub>·4 H<sub>2</sub>O, Sinopharm Chemical Reagent, ≥ 99%), sodium sulfide nonahydrate (Na<sub>2</sub>S·9 H<sub>2</sub>O, sigma-aldrich, ≥ 98%), hydrochloric acid (HCl, Sinopharm Chemical Reagent, 36.0 ~ 38.0%), sodium hydroxide (NaOH, sigma-aldrich, ≥ 98%), absolute ethanol (Sinopharm Chemical Reagent, ≥ 99.7%), urea (CO(NH<sub>2</sub>)<sub>2</sub>, Sinopharm Chemical Reagent, ≥ 99.0%) were used directly without any further treatment. The ultrapure water (18.25 MΩ cm<sup>-1</sup>) was used throughout the whole experiment.

### 2.2. Synthesis of NiMoO<sub>4</sub> precursors

First, nickel nitrate and ammonium molybdate were dispersed in 30 ml ultrapure water and then ultrasonic dispersion (30 min) and stirring (20 min) were carried out to obtain a homogenous solution containing

Ni<sup>2+</sup> and molybdate. Next, the dispersed solution with a piece of pre-treated Ni foam (NF, 1 × 4 cm<sup>2</sup>) was transferred into a Teflon reaction kettle (50 ml). The Ni foam substrate was cleaned in acetone (15 min), 0.1 M hydrochloric acid (10 min), and ethanol (15 min). Subsequently, the reaction kettle was sealed and heated at 150 °C for 6 h. After being cooled to room temperature naturally, the precursor was washed with ultrapure water and dried at 60 °C for 4 h. The above-obtained Ni-Mo-O precursor was placed in a quartz boat and transferred into the center of a tube furnace for high-temperature pyrolysis treatment. The synthesis was conducted by rising the calcination temperature from 20° to 350°C at a heating rate of 5 °C min<sup>-1</sup> and held steady at this temperature for 2 h under a flowing Ar atmosphere.

### 2.3. Synthesis of Mo-NiS/Ni<sub>3</sub>S<sub>2</sub> and Mo-NiS/Ni<sub>3</sub>S<sub>2</sub>-S<sub>v</sub>

The synthesized NiMoO<sub>4</sub> precursors were then transferred to the Teflon-lined stainless-steel autoclave containing Na<sub>2</sub>S·9 H<sub>2</sub>O solution, which was put in an electric oven immediately for subsequent hydrothermal sulfidation treatment. The treatment condition was set to constant temperature of 200 °C for 18 h. After that, the sulfurized NiMoO<sub>4</sub> precursors were immersed in 1 M HCl solution for 60 min, and then the samples were taken out and washed. The high acid concentration (2 M HCl) may corrode the skeleton of the Ni substrate and may negatively influence the stability of the electrode. The low acid concentration (0.1 M HCl) might have negligible effect on the performance of the electrode. Thus, 1 M HCl was selected as the acid etching concentration. The samples obtained in the presence of Ni (NO<sub>3</sub>)<sub>2</sub>·6 H<sub>2</sub>O (2 mmol) and (NH<sub>4</sub>)<sub>6</sub>Mo<sub>7</sub>O<sub>24</sub>·4 H<sub>2</sub>O (0.45 mmol), as well as Na<sub>2</sub>S·9 H<sub>2</sub>O (0.08 mol L<sup>-1</sup>) for sulfidation, at different acid etching times of 0, 30, 60 min and 90 min, were denoted as Mo-NiS/Ni<sub>3</sub>S<sub>2</sub>- free S<sub>v</sub>, Mo-NiS/Ni<sub>3</sub>S<sub>2</sub>- poor S<sub>v</sub>, Mo-NiS/Ni<sub>3</sub>S<sub>2</sub>- rich S<sub>v</sub> and Mo-NiS/Ni<sub>3</sub>S<sub>2</sub>- excess S<sub>v</sub>, respectively. The amounts of Ni (NO<sub>3</sub>)<sub>2</sub>·6 H<sub>2</sub>O and (NH<sub>4</sub>)<sub>6</sub>Mo<sub>7</sub>O<sub>24</sub>·4 H<sub>2</sub>O, as well as the sulfion concentration for sulfidation, are shown in the [Supplementary Information, Table S1](#).

### 2.4. Structural characterization

The powder X-ray diffraction (XRD) using Cu Kα radiation with a fixed slit was employed to characterize the phase compositions of the as-obtained samples. The field emission scanning electron microscopy (FE-SEM, Hitachi, Japan) and high-resolution transmission electron microscopy (HRTEM, JEM-2100 F, JEOL, Japan) coupled with energy dispersive X-ray (EDX) spectroscopy were conducted to examine the morphology and microstructures of these catalysts. Raman spectra were acquired using a confocal Raman microscope (inVia-Reflex, Renishaw, United Kingdom) with an excitation wavelength of 532 nm from a He-Ne laser and a power of 1–3 mW. Electron paramagnetic resonance (EPR) spectra were recorded using a JEOL JES-FA200 EPR Spectrometer. The X-ray photoelectron spectra (XPS) were collected in an ESCALAB 250Xi X-ray photoelectron spectroscope (ThermoFisher, USA) to analyze the element compositions and valence states of the catalysts, and the binding energy was calibrated against the reference of C1s peak at 284.8 eV.

### 2.5. Electrochemical characterization

The electrochemical tests for the HER, oxygen evolution reaction (OER) and urea oxidation reaction (UOR) were carried out by an electrochemical workstation (Gamry, Interface 1010E) in a three-electrode system. The prepared samples were directly used as the working electrode, while a graphite rod and an Ag/AgCl electrode serve as the counter and reference electrode, respectively. Two electrolytes containing 1 M KOH and 1 M KOH + 0.5 M urea, respectively, were used. The pH in the electrolyte was around 14. The cyclic voltammetry (CV) method was conducted to cycle these prepared electrodes until a stable polarization curve was obtained. After that, linear sweep voltammetry (LSV) was performed at a scan rate of 1 mV s<sup>-1</sup> to acquire the

polarization curve. Unless specifically noted, all of the potentials are represented without iR compensation. For standardization, all potentials mentioned in this work were calibrated to a reversible hydrogen electrode (RHE) by the equation:  $E_{\text{RHE}} = E_{\text{Ag/AgCl}} + 0.0591 \times \text{pH} + 0.198 \text{ V}$ . The faradaic efficiencies (FE) of  $\text{H}_2$  were calculated using the following equation:  $\eta_{\text{FE}} = (m \times z \times F)/Q$ , where  $m$  denotes the moles of  $\text{H}_2$  product,  $z$  denotes transferred electrons,  $F$  is the faradaic constant and  $Q$  is the consumed charge. The  $\text{H}_2$  gas produced in the cathode compartment of the H-type electrolytic cell was collected by the water drainage method at a current of 100 mA. The time were recorded every 5 ml of hydrogen collected. The estimation of the effective electrochemical surface area (ECSA) was carried out by applying cyclic voltammetry measurements at different scan rates to probe the electrochemical double-layer capacitance ( $C_{\text{dl}}$ ) in the non-faradaic region. Chronopotentiometry measurements were performed at various current densities to evaluate the long-term stability of the samples. Electrochemical impedance spectroscopy (EIS) measurements were conducted using this apparatus over a frequency range of 0.01 Hz to 100 kHz with an AC amplitude of 5 mV. The water electrolysis and urea electrolysis were conducted in a two-electrode configuration with Mo-NiS/ $\text{Ni}_3\text{S}_2$ -Sv as both cathode and anode materials.

## 2.6. In situ electrochemical Raman test

In situ Raman system were established by combining a confocal Raman microscope (inVia-Reflex, Renishaw, United Kingdom) with an

excitation wavelength of 532 nm from a He-Ne laser and a power of 1–3 mW with an electrochemical workstation. For the long-time electrolysis at controlled electrochemical potentials, Raman spectral data were collected every 100 s. The Raman electrolysis system were composed of three electrodes including working electrode, reference electrode (Ag/AgCl) and counter electrode (Pt wire), respectively. A slice of catalysts attached to the Au substrate oriented at the bottom of the cell was used as the working electrode. The electrolyte was 1 M KOH solution.

## 2.7. Computational methodology

The seven complex structures of  $\text{Ni}_3\text{S}_2$  (021), NiS (021) /  $\text{Ni}_3\text{S}_2$  (021), Mo-NiS (021) /  $\text{Ni}_3\text{S}_2$  (021), Mo-NiS (021) /  $\text{Ni}_3\text{S}_2$  (021)-S<sub>v</sub>, NiS (021) /  $\text{Ni}_3\text{S}_2$  (021) - S<sub>v</sub>, Mo-NiS (021) - S<sub>v</sub> /  $\text{Ni}_3\text{S}_2$  (021)-S<sub>v</sub>, Mo-NiS (021) /  $\text{Ni}_3\text{S}_2$  (021)- 2 S<sub>v</sub> and Mo-NiS (021)/  $\text{Ni}_3\text{S}_2$  (021) - 3 S<sub>v</sub> surfaces were built, where the vacuum space along the z direction is set to be 18 Å, which was enough to avoid interaction between the two neighbouring images. Each atom in the storage models was allowed to relax to the minimum enthalpy without any constraints. The first principles calculations in the framework of density functional theory were carried out based on the Cambridge Sequential Total Energy Package known as CASTEP [27]. The exchange-correlation function under the generalized gradient approximation (GGA) with norm-conserving pseudopotentials and Perdew-Burke-Ernzerhof function was adopted to describe the electron-electron interaction [28]. An energy cutoff of 750 eV was used and a k-point sampling set of  $5 \times 5 \times 1$  were tested to be converged. A

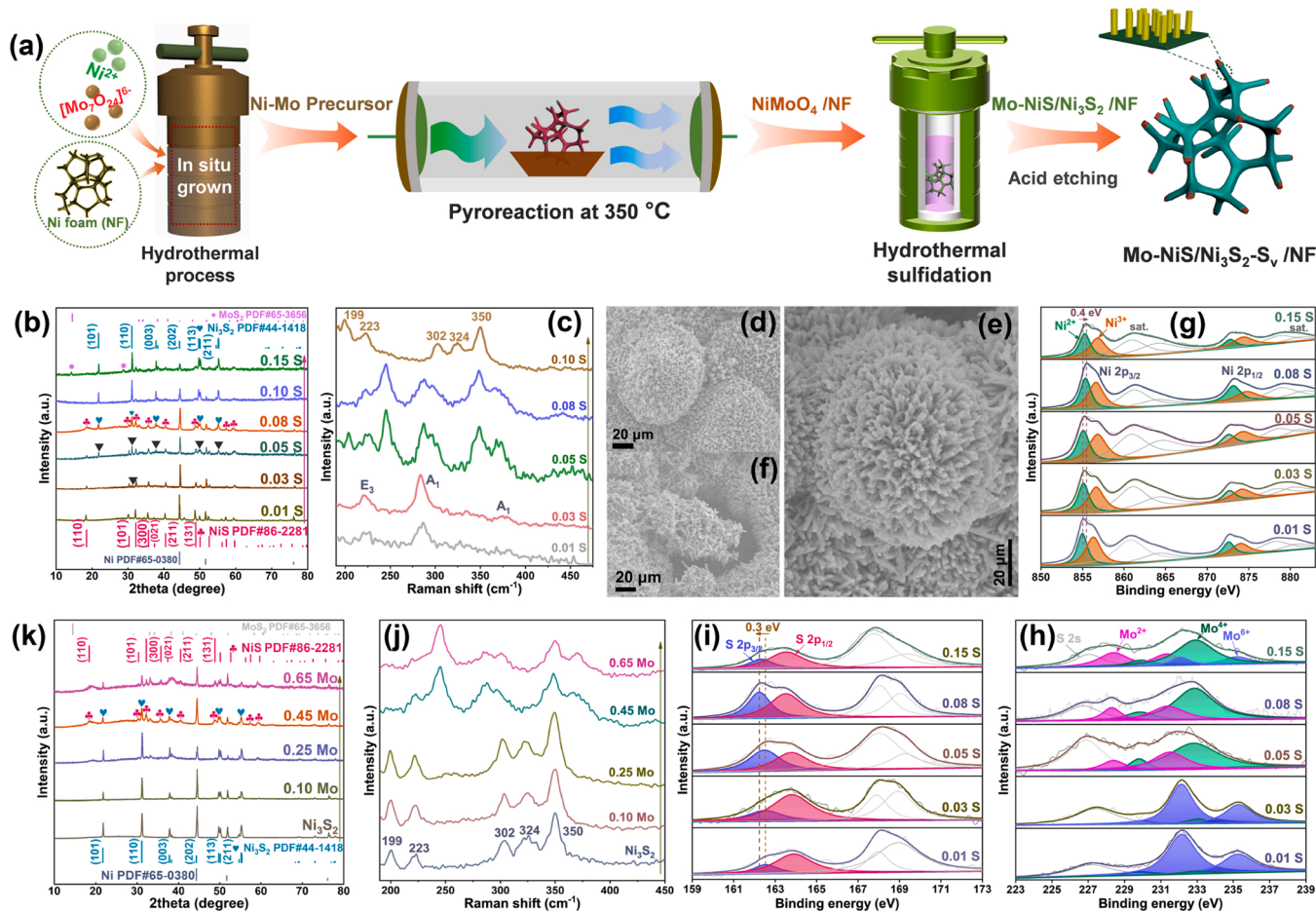


**Fig. 1.** (a) Schematic illustration of the method to synthesize the Mo-NiS/ $\text{Ni}_3\text{S}_2$  electrocatalyst with S vacancies (Mo-NiS/ $\text{Ni}_3\text{S}_2$ -S<sub>v</sub>). (b) XRD patterns and (c) Raman spectra reveal the structural phase change from NiS to NiS/ $\text{Ni}_3\text{S}_2$  to  $\text{Ni}_3\text{S}_2$  as the sulfion amounts increase. SEM images of the (d) NiS-0.01 S, (e) NiS/ $\text{Ni}_3\text{S}_2$ -0.08 S, (f)  $\text{Ni}_3\text{S}_2$ -0.15 S electrocatalysts. High-resolution XPS spectra of (g) Ni 2p, (h) Mo 3d and (i) S 2p for the as-obtained samples with various amounts of sulfion. (j) Raman spectra and (k) XRD patterns reveal the structural phase change from  $\text{Ni}_3\text{S}_2$  to NiS/ $\text{Ni}_3\text{S}_2$  as the Mo amounts increase.



force tolerance of  $0.01 \text{ eV } \text{\AA}^{-1}$ , energy tolerance of  $5.0 \times 10^{-7} \text{ eV}$  per atom and maximum displacement of  $5.0 \times 10^{-4} \text{ \AA}$  were considered (see the [Supplementary Information](#) for more details).

### 3. Results and discussion

#### 3.1. Morphology and structure characterization

Fig. 1a shows a schematic illustration of the facile synthesis method for the fabrication of the desired electrocatalysts. Firstly, the  $\text{MoNiO}_4$  cuboids grown on a piece of nickel foam were prepared. Secondly, the  $\text{MoNiO}_4$  precursors were further converted to  $\text{NiS}/\text{Ni}_3\text{S}_2$  polymorphs via a hydrothermal treatment in the presence of  $\text{Na}_2\text{S}$ . The desired  $\text{NiS}/\text{Ni}_3\text{S}_2$  electrocatalyst was finally achieved by an etching approach using  $0.1 \text{ M}$   $\text{HCl}$  solution. The phase composition of the as-prepared samples was first examined by means of X-ray diffraction (XRD). In terms of XRD

patterns of a  $\text{NiS}/\text{Ni}_3\text{S}_2$  precursor, the characteristic peaks were well ascribed to the  $\text{MoNiO}_4$  phase (PDF#86-0361) (Fig. S2) [29]. After sulfurization with a low concentration of sulfion ( $\text{S}^{2-}$ ), the typical diffraction peaks at  $18.4^\circ$ ,  $30.3^\circ$ ,  $32.2^\circ$ ,  $35.7^\circ$  and  $57.4^\circ$  were well-indexed to the reference XRD pattern of  $\text{NiS}$  with a space group of  $R\bar{3}m$  (PDF#86-2281,  $a = b = 9.62 \text{ \AA}$ ,  $c = 3.15 \text{ \AA}$ ) (Fig. 1b) [30]. With sulfion concentration elevation, new XRD characteristic peaks (black arrows) that belongs to  $\text{Ni}_3\text{S}_2$  started to emerge. When the sulfion concentration further increased to  $0.08 \text{ M}$ , the predominant peaks located at  $21.7^\circ$ ,  $31.1^\circ$ ,  $37.8^\circ$  and  $55.2^\circ$ , assigned to the (101), (110), (003) and (122) planes of  $\text{Ni}_3\text{S}_2$ , were intensified, confirming the formation of a mixed phase in the  $\text{NiS}/\text{Ni}_3\text{S}_2$  heterostructure. Interestingly, excessive sulfurization gave rise to the disappearance of the  $\text{NiS}$  phase and the XRD pattern finally matched well to the rhombohedral crystal structure of  $\text{Ni}_3\text{S}_2$  (PDF#44-1418,  $a = b = 5.74 \text{ \AA}$ ,  $c = 7.13 \text{ \AA}$ ) [31]. In addition, two shoulders at a 2-theta position of around  $35.0^\circ$  and  $42.3^\circ$  (pink

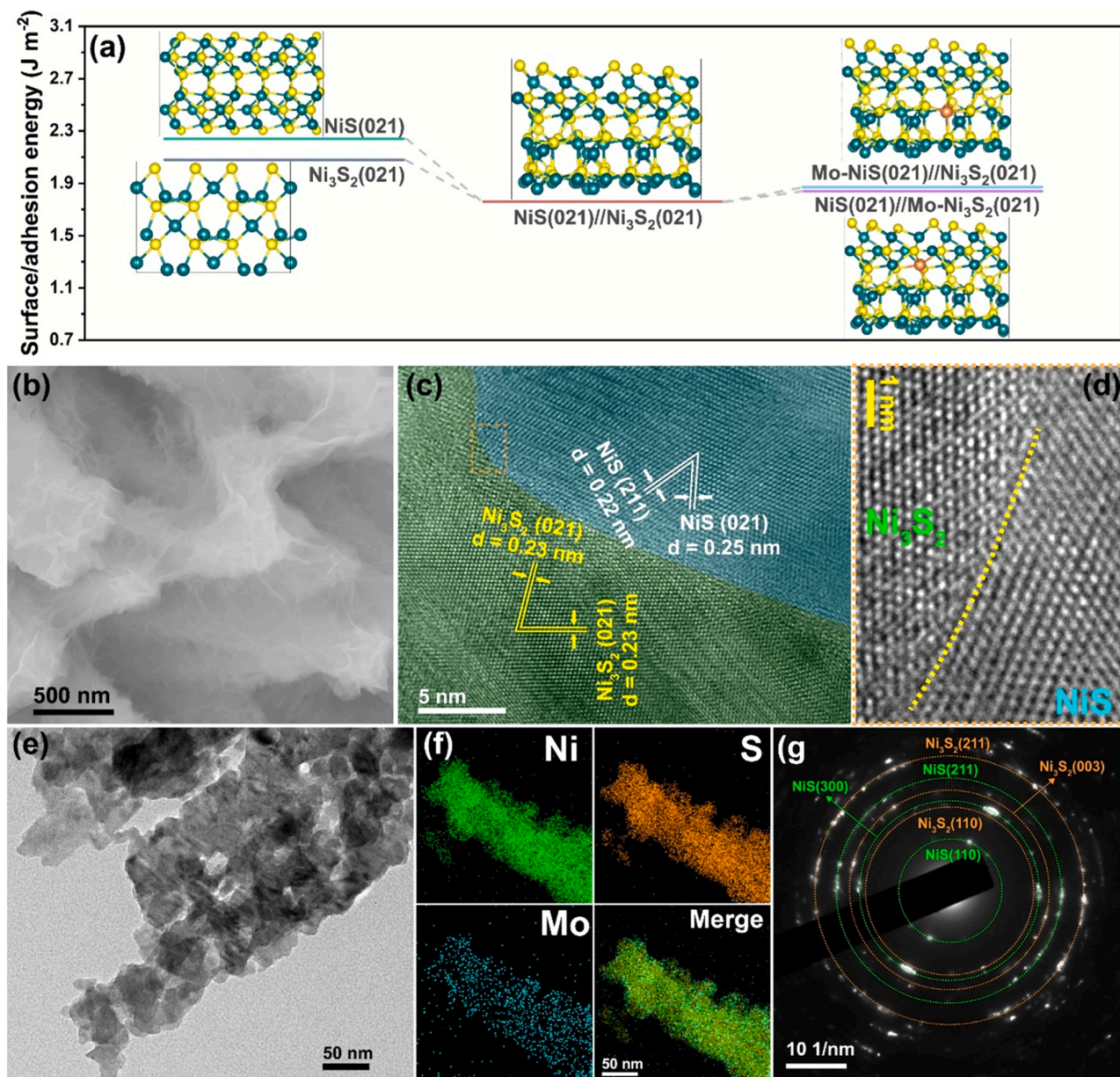


**Fig. 2.** (a) Surface/adhesion energy diagrams of  $\text{NiS}(021)$ ,  $\text{Ni}_3\text{S}_2(021)$ ,  $\text{NiS}(021)/\text{Ni}_3\text{S}_2(021)$ ,  $\text{Mo-NiS}(021)/\text{Ni}_3\text{S}_2(021)$  and  $\text{NiS}(021)/\text{Mo-Ni}_3\text{S}_2(021)$ , respectively. (b) Magnified SEM image of the  $\text{Mo-NiS}/\text{Ni}_3\text{S}_2$ -0.08 S electrocatalyst. (c-d) HRTEM images of the  $\text{Mo-NiS}/\text{Ni}_3\text{S}_2$ -0.08 S electrocatalyst. A heterointerface is marked with yellow dotted lines. (e) TEM image of the  $\text{Mo-NiS}/\text{Ni}_3\text{S}_2$ -0.08 S electrocatalyst. (f) The corresponding EDS elemental mapping images of Ni, S and Mo elements. (g) The SAED pattern of the  $\text{NiS}/\text{Ni}_3\text{S}_2$ -0.08 S electrocatalyst.



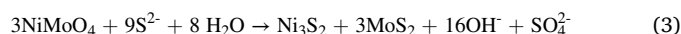
circles), corresponding to a MoS<sub>2</sub> phase, were observed with the successive addition of sulfion.

Raman spectroscopy was also performed to characterize the as-prepared samples. Three typical peaks appeared at 225, 283 and 377 cm<sup>-1</sup> were attributable to the E<sub>2g</sub>, A<sub>1g</sub> and A<sub>1g</sub> stretching mode of NiS, as depicted in Fig. 1c [32]. After increasing the sulfion concentration, the Raman spectrum showed the emergence of new Raman bands at 223, 302, and 350 cm<sup>-1</sup>, assigned to Ni-S bonds of Ni<sub>3</sub>S<sub>2</sub>, while the NiS peaks were well preserved, suggesting the presence of both phases [33]. The Raman spectra also revealed that the NiS peaks vanished and the Ni<sub>3</sub>S<sub>2</sub> phase became the dominant structure after excessive sulfurization, which was in close accordance with the XRD results described above. Thus, significant NiS → Ni<sub>3</sub>S<sub>2</sub> phase transition was clearly induced by the progressive increase of sulfion in the hydrothermal treatment. Notably, the pyrite-type NiS<sub>2</sub> phase was invisible probably because the spread of Ni-S bond distances (2.25–2.28 Å) in Ni<sub>3</sub>S<sub>2</sub> was similar to that (2.25–2.32 Å) in NiS but shorter than that (2.35–2.38 Å) in NiS<sub>2</sub>. Besides, the NiS<sub>2</sub> was commonly synthesized by high-temperature sulfurization under an inert atmosphere.[23] The morphology of the samples obtained under different sulfion concentrations was observed by scanning electron microscopy (SEM). The SEM images showed that the flower-like NiMoO<sub>4</sub> precursor, consisted of cuboids with lengths of tens of microns, were vertically arranged on the NF (Fig. S3). After the sulfurization treatment with a low concentration of sulfion, the derived NiS retained a flower-like morphology but lost the cuboid structure (Fig. 1d). In the case of the NiS/Ni<sub>3</sub>S<sub>2</sub>, the flower-like structure of the original NiMoO<sub>4</sub> was inherited by the derived NiS/Ni<sub>3</sub>S<sub>2</sub>. A closer inspection of these flowers under high-resolution SEM presented a structure of nanorod arrays with numerous fuzzy flakes (Figs. 1e, 2b and S4). The well aligned arrays grown on the NF were believed to provide efficient diffusion pathways for electrolyte and open channels for the release of gaseous products. For the obtained Ni<sub>3</sub>S<sub>2</sub> samples, excessive sulfurization appeared to lead to the collapse of the flower-like structure (Fig. 1f).

X-ray photoelectron spectroscopy (XPS) was employed to investigate the surface composition and chemical valence states of the fabricated sulfides. The high-resolution Ni 2p spectrum shown in Fig. 1g clearly displayed the strong Ni 2p<sub>3/2</sub> and 2p<sub>1/2</sub> peaks, respectively, as well as their satellite peaks, on the nickel sulfide samples. After deconvolution, the Ni 2p profiles exhibited the dual characteristics of two spin orbits of Ni<sup>2+</sup> and Ni<sup>3+</sup>. For the NiS sample, two main peaks at 855.0 and 872.6 eV belonged to Ni<sup>2+</sup>, while the peaks at 856.3 and 874.1 eV were vested in Ni<sup>3+</sup> [34]. In the case of Ni<sub>3</sub>S<sub>2</sub>, however, the Ni<sup>2+</sup> peaks were located at 855.3 and 872.8 eV and the Ni<sup>3+</sup> centered at 856.7 and 874.4 eV [35,36]. Interestingly, compared with NiS and Ni<sub>3</sub>S<sub>2</sub>, the Ni<sup>2+</sup> binding energies of the NiS/Ni<sub>3</sub>S<sub>2</sub> at 855.4 eV presented a positive shift, suggesting a lower electron density around Ni atoms in the NiS/Ni<sub>3</sub>S<sub>2</sub> heterostructure. The S 2p spectra of nickel sulfide were fitted with four peaks in Fig. 1i. Among them, two peaks at 162.3 and 163.5 eV were assigned to S 2p<sub>3/2</sub> and S 2p<sub>1/2</sub> of divalent sulfide ions (S<sup>2-</sup>), respectively, while other bands at 168.0 and 169.1 eV were attributed to sulfate species formed by further oxidation of the sulfide ions [36]. Importantly, the peaks assigned to S 2p<sub>3/2</sub> (162.3 eV) and S 2p<sub>1/2</sub> (163.5 eV) of NiS/Ni<sub>3</sub>S<sub>2</sub> were shifted to the lower binding energy compared with those of NiS (162.6 eV, 163.9 eV) and Ni<sub>3</sub>S<sub>2</sub> (162.4 eV, 163.6 eV), suggesting an increased electron density around the sulfur atom. Based on the results above, the Ni 2p and S 2p in the NiS/Ni<sub>3</sub>S<sub>2</sub> were positively- and negatively-shifted compared with NiS and Ni<sub>3</sub>S<sub>2</sub>, suggesting the antidromic electron transfer from Ni to adjacent S sites in the NiS/Ni<sub>3</sub>S<sub>2</sub> heterostructures. The rich electron density around S sites may trigger a strong adsorption of hydrogen intermediates and favor HER. It should be noted that the Mo (VI) in the NiMoO<sub>4</sub> precursor was reduced to the low-valence Mo (IV, II) with increase of sulfion concentration, which might be ascribed to sulfur bonding to Mo to form molybdenum sulfide, indicating the presence of Mo doping in the NiS/Ni<sub>3</sub>S<sub>2</sub> heterostructures (Fig. 1h) [37].

The influence of Mo/Ni ratio on the formation of NiS/Ni<sub>3</sub>S<sub>2</sub> heterostructure was subsequently investigated. It was found that in the absence of Mo, the well-defined diffraction peaks assigned to rhombohedral Ni<sub>3</sub>S<sub>2</sub> were only observed (Fig. 1k). After elevating the Mo amount, mixed crystals of NiS/Ni<sub>3</sub>S<sub>2</sub> were achieved with the appearance of the NiS phase. The variation of crystal phase of the samples was further verified by Raman spectroscopy (Fig. 1j). Moreover, SEM observation of the sulfides revealed that the Mo amount had a significant effect on the flower-like morphology (Fig. S5). XPS analysis also uncovered a positive shift of Ni 2p and negative shift of S 2p for the NiS/Ni<sub>3</sub>S<sub>2</sub> compared with that of the Ni<sub>3</sub>S<sub>2</sub> (Figs. S6a and 6b). The high-resolution Mo 3d portion of the XPS spectra indicated that the low-valence Mo (II, IV) were the dominant species in the samples (Fig. S6c) [38].

Based on the above XRD, Raman and XPS analyses, it was clear that the sulfion concentration and Mo amount played paramount roles in the interface formation between the two nickel sulfide polymorphs. The possible formation mechanism for the polymorph interface can be described by the following reactions:



At low concentrations of sulfion, sulfurization mainly takes place through reactions (1) and (2). In aqueous conditions, the sulfion (S<sup>2-</sup>) is hydrolyzed to produce HS<sup>-</sup>, which reacts with NiMoO<sub>4</sub> precursors to generate NiS as the main product, and MoO<sub>3</sub> as the side product [39]. With the increase of the sulfion concentration, S<sup>2-</sup> anions became the dominant species that give rise to reaction (3) [39]. In this case, the NiMoO<sub>4</sub> precursor is sulfurized by S<sup>2-</sup> into Ni<sub>3</sub>S<sub>2</sub>, with the side product of MoS<sub>2</sub>. In absence of Mo, the precursor is more readily sulfurized by S<sup>2-</sup> to Ni<sub>3</sub>S<sub>2</sub> instead of NiS. Hence, in the presence of appropriate sulfion and Mo amounts, both Ni<sub>3</sub>S<sub>2</sub> and NiS will be produced and heterogenous interfaces are thereby created.

Density functional theory (DFT) calculation was conducted to verify the feasibility of the polymorph interface. The adhesion energy (W<sub>ad</sub>) is calculated to determine the energetically stable interface. The positive value of W<sub>ad</sub> means that the interface is energetically favorable over the free surfaces and the model with larger W<sub>ad</sub> will be more stable [40]. The calculated W<sub>ad</sub> of NiS (021)/Ni<sub>3</sub>S<sub>2</sub> (021) was 1.759 J m<sup>-2</sup>, smaller than the sum surface energies of NiS (021) (2.239 J m<sup>-2</sup>) and Ni<sub>3</sub>S<sub>2</sub> (021) (2.079 J m<sup>-2</sup>), suggesting that the epitaxial growth of NiS or Ni<sub>3</sub>S<sub>2</sub> was thermodynamically favored (Fig. 2a and Table S2). Besides, the W<sub>ad</sub> of Mo-NiS (021)/ Ni<sub>3</sub>S<sub>2</sub> (021) (1.871 J m<sup>-2</sup>) and NiS (021)/Mo-Ni<sub>3</sub>S<sub>2</sub> (021) (1.839 J m<sup>-2</sup>) were larger than that of NiS (021)/Ni<sub>3</sub>S<sub>2</sub> (021), revealing that the introduction of Mo could stabilize the polymorph interface of NiS/Ni<sub>3</sub>S<sub>2</sub> (Fig. 2a and Table S3). The heterointerface structure between Ni<sub>3</sub>S<sub>2</sub> and NiS was further examined by high-resolution transmission electron microscopy (HRTEM). As shown in Fig. 2c, interfaces that demonstrated two phases with different crystal structures were observed under HRTEM. The lattice fringes were vague at the interface region, reflecting the mis-arrangement of atoms at interfaces. The lattice fringes with interplanar spacings of 0.22 and 0.25 nm corresponded well to the (211) and (021) facets of NiS, respectively. In the other region, the interplanar spacings of 0.23 nm can be indexed to the (021) plane of Ni<sub>3</sub>S<sub>2</sub>. An interface between the (021) planes of NiS and Ni<sub>3</sub>S<sub>2</sub> can also be observed by matching the lattice fringes of both sides of the interface (Fig. 2d). The TEM image of the NiS/Ni<sub>3</sub>S<sub>2</sub> shown in Fig. 2e exhibited a nanorods structure with an average diameter of around 100 nm, and the nanorods were composed of stacked nanoparticles. The scanning TEM (STEM) image and corresponding energy-dispersive X-ray spectroscopy (EDS) elemental mapping indicated the uniform distribution of Ni, S and Mo elements throughout the whole structure (Fig. 2f). The selected area electron diffraction (SAED) pattern further confirmed the existence of

rhombohedral NiS and rhombohedral Ni<sub>3</sub>S<sub>2</sub> in the polymorphs (Fig. 2g). The microstructures of the other sulfides were also investigated by TEM, and their corresponding information are given in the Supporting Information (Fig. S7 - S10).

### 3.2. Electrochemical HER activity

The electrocatalytic activity of the as-prepared nickel sulfide samples for HER was investigated in 1 M KOH solution using a typical three-electrode system with the graphite rod as the counter electrode. Fig. 3a displays the linear sweep voltammetry (LSV) curves of the catalysts obtained at a scan rate of 1 mV s<sup>-1</sup> without iR compensation as well as commercial Pt plate. Clearly, the HER activity of the used NF substrate and Pt plate was low. Compared with the NiS sample with a poor catalytic activity, the various Mo-NiS/Ni<sub>3</sub>S<sub>2</sub> samples exhibited significant enhancements in the HER activities. The Mo-NiS/Ni<sub>3</sub>S<sub>2</sub>-0.08 S sample demonstrated the best HER activity among these samples, requiring only 73 mV to achieve the current density of 10 mA cm<sup>-2</sup>. Notably, the Mo-NiS/Ni<sub>3</sub>S<sub>2</sub>-0.08 S sample presented a low overpotential of 230 mV at the high current density of 100 mA cm<sup>-2</sup>, which was superior to that of Mo-NiS-0.01 S (322 mV), Mo-NiS/Ni<sub>3</sub>S<sub>2</sub>-0.03 S (300 mV), Mo-NiS/Ni<sub>3</sub>S<sub>2</sub>-0.05 S (253 mV), Ni<sub>3</sub>S<sub>2</sub> (283 mV) electrocatalysts (Fig. 3b). After iR compensation, the overpotential of the Mo-NiS/Ni<sub>3</sub>S<sub>2</sub>-0.08 S electrocatalyst decreased to 167 mV at 100 mA cm<sup>-2</sup> (Fig. S11). Furthermore, Tafel plots constructed from steady polarization curves were employed to shed light on the HER kinetics. As indicated in Fig. 3b, the Mo-NiS/Ni<sub>3</sub>S<sub>2</sub>-0.08 S sample exhibited a Tafel slope of 115.7 mV dec<sup>-1</sup>, which showed a more rapid HER kinetics than that of Mo-NiS-0.01 S (322 mVdec<sup>-1</sup>) and Ni<sub>3</sub>S<sub>2</sub> (283 mVdec<sup>-1</sup>) electrocatalysts, as well as the Mo-NiS/Ni<sub>3</sub>S<sub>2</sub>-0.03 S (300 mVdec<sup>-1</sup>), Mo-NiS/Ni<sub>3</sub>S<sub>2</sub>-0.05 S (253 mVdec<sup>-1</sup>) electrocatalysts, following the Volmer-Heyrovsky mechanism.

The charge transfer resistances of the nickel sulfide electrocatalysts

were then evaluated by means of electrochemical impedance spectroscopy (EIS). Using a simplified circuit model composed of electrolyte resistance ( $R_s$ ), a constant phase element (CPE) and charge transfer resistance ( $R_{ct}$ ), the  $R_{ct}$  of Mo-NiS/Ni<sub>3</sub>S<sub>2</sub>-0.08 S was estimated to be 3.33  $\Omega$ , which is much smaller than the other electrocatalysts (Fig. 3c, S12 and Table S4). The low charge transfer resistance revealed the rapid HER kinetics at the electrocatalyst/electrolyte interface. The double-layer capacitance ( $C_{dl}$ ) was then measured to roughly estimate the effective electrochemically active surface area (ECSA) of the studied electrocatalysts. The  $C_{dl}$  value of the Mo-NiS/Ni<sub>3</sub>S<sub>2</sub>-0.08 S electrocatalyst was also the largest among these electrocatalysts, suggesting more accessible active centers in the Mo-NiS/Ni<sub>3</sub>S<sub>2</sub>-0.08 S electrocatalyst (Fig. 3d and S13). The turnover frequency (TOF) and mass activity of the nickel sulfides electrodes were also compared to assess the specific activities. The calculated TOF for Mo-NiS/Ni<sub>3</sub>S<sub>2</sub>-0.08 S is up to 0.763 s<sup>-1</sup>, which is the highest among these nickel sulfides at the overpotential of 200 mV (Fig. S14a). The result is in good agreement with the trends of mass activity (Fig. S14b). In addition, the faradaic efficiency (FE) of the Mo-NiS/Ni<sub>3</sub>S<sub>2</sub>-0.08 S electrocatalyst towards the alkaline HER was calculated by comparison of the amount of experimentally quantified gas with the theoretically calculated gas, which gave an average FE of 99.16% (Fig. S15 and Table S5). The HER performance of Mo-NiS/Ni<sub>3</sub>S<sub>2</sub>-0.08 S electrodes with various Mo/Ni ratios was also assessed, and this indicated that the Mo-NiS/Ni<sub>3</sub>S<sub>2</sub>-0.08 S electrocatalyst possessed the optimal HER activity (Fig. S16). The catalytic stability of the Mo-NiS/Ni<sub>3</sub>S<sub>2</sub>-0.08 S electrocatalyst under the HER working condition was also examined by the accelerated degradation test and chronoamperometry. After conducting reduplicative cyclic voltammograms for 1000 cycles, as displayed in Fig. 3e, the Mo-NiS/Ni<sub>3</sub>S<sub>2</sub>-0.08 S electrocatalyst was found to retain a high catalytic activity. No significant potential decay was observed after 30 h of continuous hydrogen release at current densities of 100, 50 and 10 mA cm<sup>-2</sup>. Post characterizations were further employed to examine

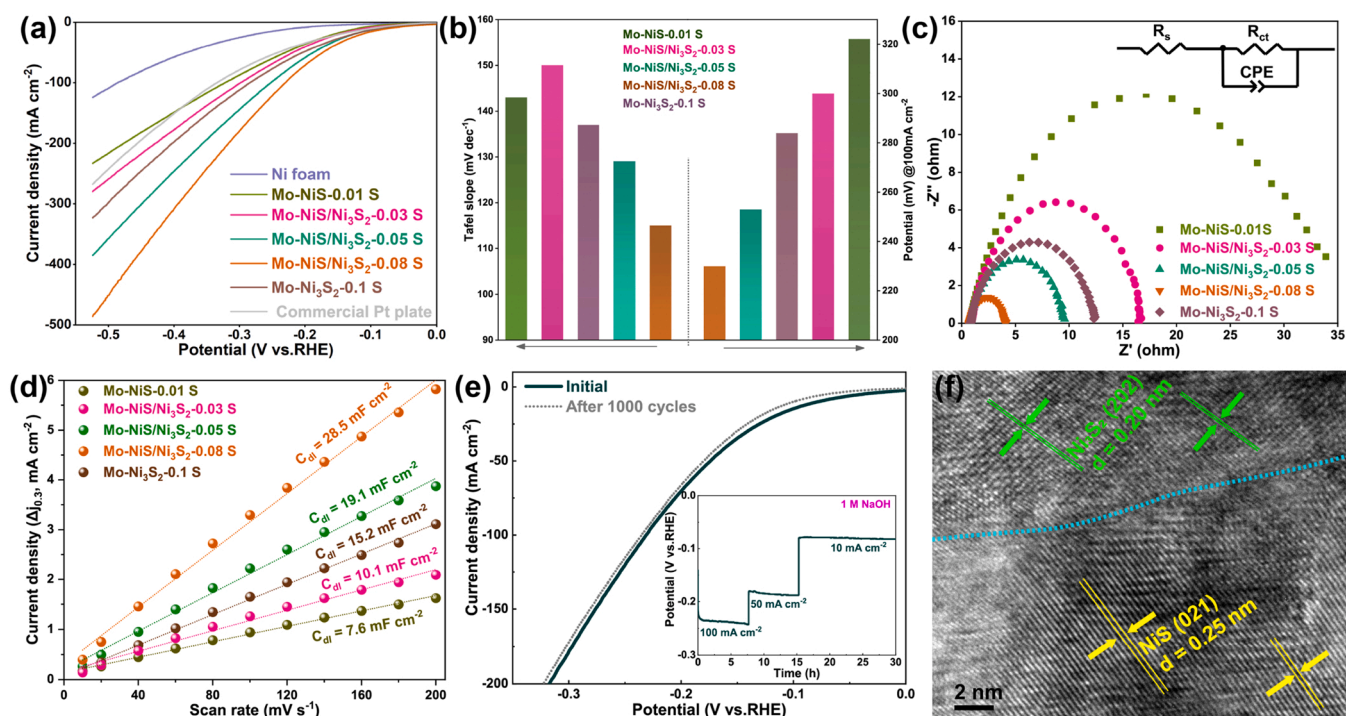


**Fig. 3.** (a) HER polarization curves of various Mo-NiS/Ni<sub>3</sub>S<sub>2</sub>-S and Ni foam samples (without iR correction, scanning rate: 1 mV s<sup>-1</sup>). (b) Comparison of Tafel slopes and potentials required to reach  $j = 100 \text{ mA cm}^{-2}$ , and for the as-obtained nickel sulfide electrocatalysts. (c) EIS Nyquist plots for the Mo-NiS/Ni<sub>3</sub>S<sub>2</sub>-S samples. Inset shows equivalent circuit model for fitting EIS data. (d) The  $C_{dl}$  values of the Mo-NiS/Ni<sub>3</sub>S<sub>2</sub>-S samples. (e) Polarization curves for the Mo-NiS/Ni<sub>3</sub>S<sub>2</sub>-0.08 S electrocatalyst before and after 1000 cycles. Inset shows the stability test for 30 h. (f) HRTEM image of the Mo-NiS/Ni<sub>3</sub>S<sub>2</sub>-0.08 S electrocatalyst after 30 h durability testing, showing that the heterointerface was maintained.



the surface structure and chemical compositions of the Mo-NiS/Ni<sub>3</sub>S<sub>2</sub>-0.08 S electrocatalyst after the HER stability test. Analysis by SEM and TEM showed no obvious change to the morphology and crystal structure of the Mo-NiS/Ni<sub>3</sub>S<sub>2</sub>-0.08 S electrocatalyst (Fig. S17). In particular, the lattice-matched atomic interface was still preserved after long-term activation (Fig. 3 f). Meanwhile, the variation in chemical composition that was identified by the XRD and XPS analyses of the Mo-NiS/Ni<sub>3</sub>S<sub>2</sub>-0.08 S electrocatalyst was negligible (Fig. S18). These results suggested that the electrocatalyst displayed an outstanding robustness toward the alkaline HER.

The above results have demonstrated that the heterostructure construction in the Mo-NiS/Ni<sub>3</sub>S<sub>2</sub>-0.08 S electrocatalysts was an effective approach to boost the HER activity. In addition, it was found that the sulfur defects could be introduced into the Mo-NiS/Ni<sub>3</sub>S<sub>2</sub>-0.08 S electrocatalyst by the hydrochloric acid etching process, which was exclusively confirmed by electron paramagnetic resonance (EPR) spectroscopy. Clearly, the EPR spectra delivered an enhanced resonance peak at  $g = 2.003$  with an extended time of acid etching (Fig. 4a) [41].

The acid environment can provide the rich proton around the nickel sulfides and unsaturated S atoms on the surface of nickel sulfides can capture protons from the acidic solution to form H<sub>2</sub>S, resulting in the S vacancies. The four groups of Mo-NiS/Ni<sub>3</sub>S<sub>2</sub>-0.08 S were presented with free, relatively poor, and rich S-vacancies, and for convenience, denoted as, 'Mo-NiS/Ni<sub>3</sub>S<sub>2</sub>-free S<sub>v</sub>', 'Mo-NiS/Ni<sub>3</sub>S<sub>2</sub>-poor S<sub>v</sub>', 'Mo-NiS/Ni<sub>3</sub>S<sub>2</sub>-rich S<sub>v</sub>' and 'Mo-NiS/Ni<sub>3</sub>S<sub>2</sub>-excess S<sub>v</sub>', respectively. Specifically, the Mo-NiS/Ni<sub>3</sub>S<sub>2</sub>-free S<sub>v</sub> and Mo-NiS/Ni<sub>3</sub>S<sub>2</sub>-excess S<sub>v</sub> electrocatalyst presented an inferior HER activity with a high overpotential of 262 mV and 248 at 100 mA cm<sup>-2</sup>, respectively (Fig. 4b). The Mo-NiS/Ni<sub>3</sub>S<sub>2</sub>-rich S<sub>v</sub> exhibited a better HER performance among these etched electrocatalysts, requiring an overpotential of 230 mV to achieve a current density of 100 mA cm<sup>-2</sup> (Fig. 4b and S19). This meant that the introduction of suitable S-vacancies into the Mo-NiS/Ni<sub>3</sub>S<sub>2</sub>-0.08 S electrocatalyst was favorable for improving the catalytic activity for the HER. The low overpotentials were also comparable with those of the other non-precious HER catalysts (Fig. 4c and Table S4), including recently reported excellent electrocatalysts, 6B-Fe<sub>7</sub>S<sub>8</sub>/FeS<sub>2</sub>/NF (207 mV) [16],

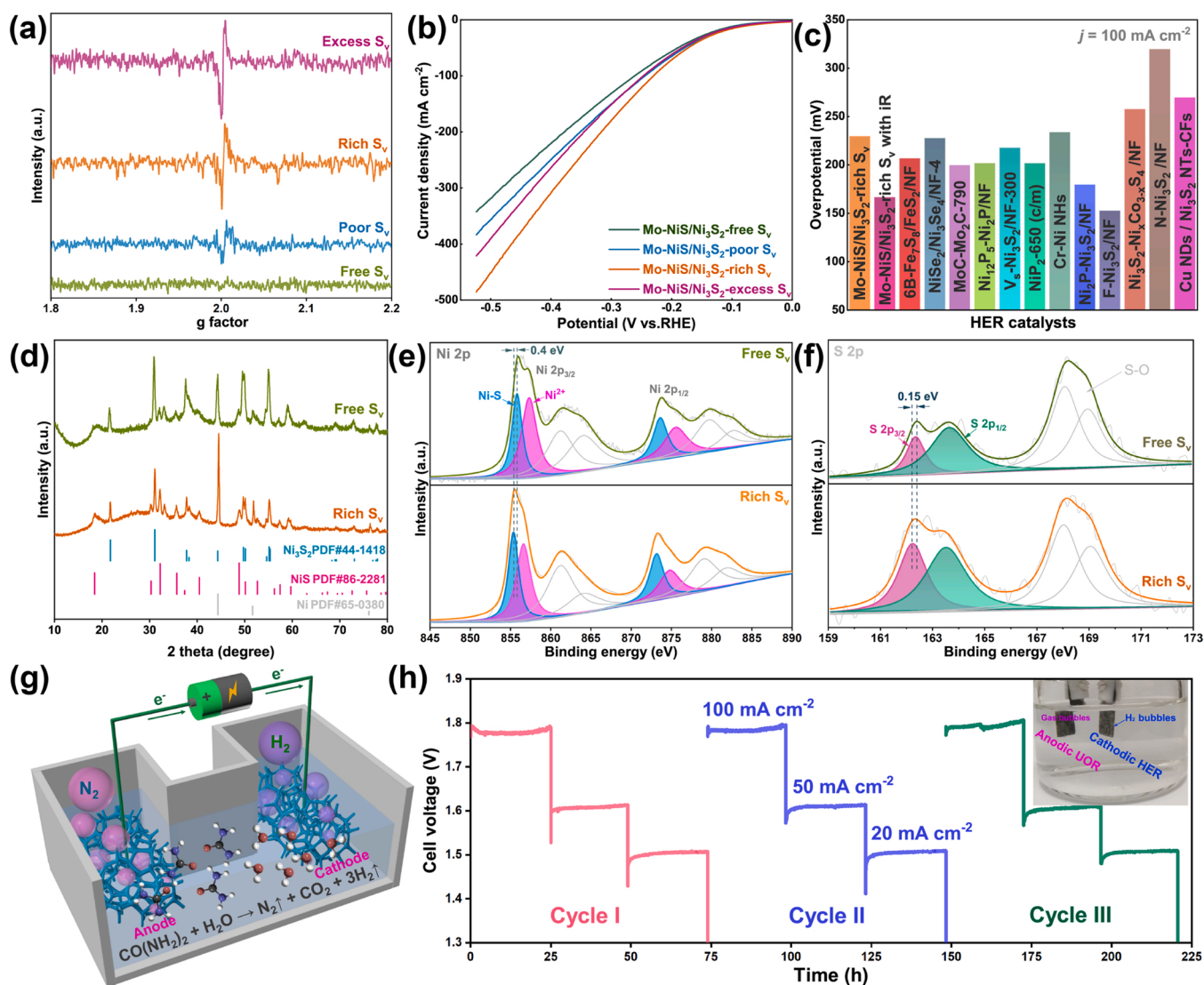


**Fig. 4.** (a) EPR spectra and (b) LSV curves of the Mo-NiS/Ni<sub>3</sub>S<sub>2</sub>-free S<sub>v</sub>, Mo-NiS/Ni<sub>3</sub>S<sub>2</sub>-poor S<sub>v</sub>, Mo-NiS/Ni<sub>3</sub>S<sub>2</sub>-rich S<sub>v</sub> (Mo-NiS/Ni<sub>3</sub>S<sub>2</sub>-0.08 S) and Mo-NiS/Ni<sub>3</sub>S<sub>2</sub>-excess S<sub>v</sub> electrocatalysts. (c) Comparison of the overpotentials required to drive the current density of 100 mA cm<sup>-2</sup> for our catalyst and available reported HER catalysts. (d) XRD pattern of the Mo-NiS/Ni<sub>3</sub>S<sub>2</sub>-free S<sub>v</sub> and Mo-NiS/Ni<sub>3</sub>S<sub>2</sub>-rich S<sub>v</sub> electrocatalysts. High-resolution XPS spectra of (e) Ni 2p and (f) S 2p for the Mo-NiS/Ni<sub>3</sub>S<sub>2</sub>-free S<sub>v</sub> and Mo-NiS/Ni<sub>3</sub>S<sub>2</sub>-rich S<sub>v</sub> electrocatalysts. (g) Schematic illustration of the overall urea splitting cell in a two-electrode system. (h) Multi-chronoamperometric response curve of the overall urea splitting using Mo-NiS/Ni<sub>3</sub>S<sub>2</sub>-rich S<sub>v</sub> as bifunctional catalyst. Inset shows the optical photograph of urea electrolysis in 1 M KOH with 0.5 M urea at 100 mA cm<sup>-2</sup>.

MoC-Mo<sub>2</sub>C-790 (200 mV) [19], Ni<sub>12</sub>P<sub>5</sub>-Ni<sub>2</sub>P/NF (202 mV) [42] and so forth. Then, XRD, Raman, SEM, and XPS characterizations were further performed to systematically compare the structural differences. The comparison from the XRD and Raman data of the electrocatalysts before and after acid etching showed negligible peak difference (Fig. 4d and S20). The SEM images indicated the flower-like morphology was well preserved after acid etching (Fig. S21). Moreover, the low-valence Mo (IV, II) of the Mo-NiS/Ni<sub>3</sub>S<sub>2</sub>-free S<sub>v</sub> was also observed from the high-resolution Mo 3d portion (Figure S22). Nevertheless, the high-resolution S 2p and Ni 2p XPS spectra indicated that the S 2p<sub>3/2</sub> and Ni 2p<sub>3/2</sub> peaks after acid etching exhibited an appreciable shift, which was probably related to the formation of S vacancies in the Mo-NiS/Ni<sub>3</sub>S<sub>2</sub>-rich S<sub>v</sub> electrocatalyst (Figs. 4e and 4f).

### 3.3. Electrocatalytic performance for urea splitting

To construct an electrolyzer for efficient H<sub>2</sub> evolution, an active anode is simultaneously needed. In view of the sluggish kinetics and high energy barrier, the anodic oxygen evolution reaction (OER) could be replaced with more readily oxidizable species than water molecules. The thermodynamics voltage of urea electrolysis (0.37 V) in alkaline media is much lower than that of water electrolysis (1.23 V), offering an ideal anodic reaction to promote hydrogen production with reduced energy consumption [9]. Fortunately, the developed Mo-NiS/Ni<sub>3</sub>S<sub>2</sub>-rich S<sub>v</sub> electrode also exhibited a superior activity toward urea oxidation reaction (UOR), with a low potential of 1.46 V to drive the current density of 100 mA cm<sup>-2</sup>, much lower than the value of 1.61 V for OER (Fig. S23a-b). The multistep chronopotentiometric curve of the Mo-NiS/Ni<sub>3</sub>S<sub>2</sub>-rich S<sub>v</sub> electrode demonstrated that the electrode possessed excellent stability for over 25 h (Fig. S23c). Consequently, a two-electrode configuration performed in 1 M KOH with 0.5 M urea was assembled using Mo-NiS/Ni<sub>3</sub>S<sub>2</sub>-rich S<sub>v</sub> as bifunctional catalyst for urea splitting (Fig. 4g). The urea electrolyzer required cell voltages of 1.40

and 1.61 V to achieve current densities of 10 and 50 mA cm<sup>-2</sup>, respectively (Fig. S24). However, to attain the same catalytic current in the absence of urea, higher voltages of 1.49 and 1.78 V were required in this system. The multi-step chronoamperometry curves in the two-electrode system were determined over a wide current density from 20 to 100 mA cm<sup>-2</sup>. The results showed that the urea electrolyzer could remain extremely stable through three cycles over 9 days, demonstrating the excellent robustness and promising application of the system (Fig. 4h). It was found that some sulfur defects in Mo-NiS/Ni<sub>3</sub>S<sub>2</sub>-rich S<sub>v</sub> could be preserved after the long-term stability test at cathode (Fig. S25). As for the anode, the flower-like morphology and the heterostructure for the Mo-NiS/Ni<sub>3</sub>S<sub>2</sub>-rich S<sub>v</sub> could be observed after the UOR durability test (Fig. S26a-d). Nevertheless, the chemical composition for the Mo-NiS/Ni<sub>3</sub>S<sub>2</sub>-rich S<sub>v</sub> underwent some changes due to the long-term oxidation (Figure S26e-g). In addition, a large quantity of gas bubbles was generated and clearly observed on both electrodes in the presence of urea (Inset of Fig. 4h and Video S1).

Supplementary material related to this article can be found online at [doi:10.1016/j.apcatb.2022.122144](https://doi.org/10.1016/j.apcatb.2022.122144).

### 3.4. Elucidation of HER mechanism

To better understand the role of the S<sub>v</sub> in the HER performance, the HER process of the Mo-NiS/Ni<sub>3</sub>S<sub>2</sub>-rich S<sub>v</sub> and Mo-NiS/Ni<sub>3</sub>S<sub>2</sub>-free S<sub>v</sub> electrodes was studied further via in situ Raman spectroscopy. Figs. 5a and 5b illustrate the Raman spectra acquired at the same position of the Mo-NiS/Ni<sub>3</sub>S<sub>2</sub>-rich S<sub>v</sub> or free S<sub>v</sub> electrode as a function of the applied potential in alkaline electrolyte. A small peak at around 2570 cm<sup>-1</sup> was observed for the Mo-NiS/Ni<sub>3</sub>S<sub>2</sub>-free S<sub>v</sub> when the potential gradually decreased from -1.00 to -1.20 V versus Ag/AgCl. The band detected at 2570 cm<sup>-1</sup> was attributed to the stretching vibration of S-H bonds, indicating that the H atom could be directly bonded to the S atom of the Mo-NiS/Ni<sub>3</sub>S<sub>2</sub>-free S<sub>v</sub> during the HER [8,43]. With the potential further

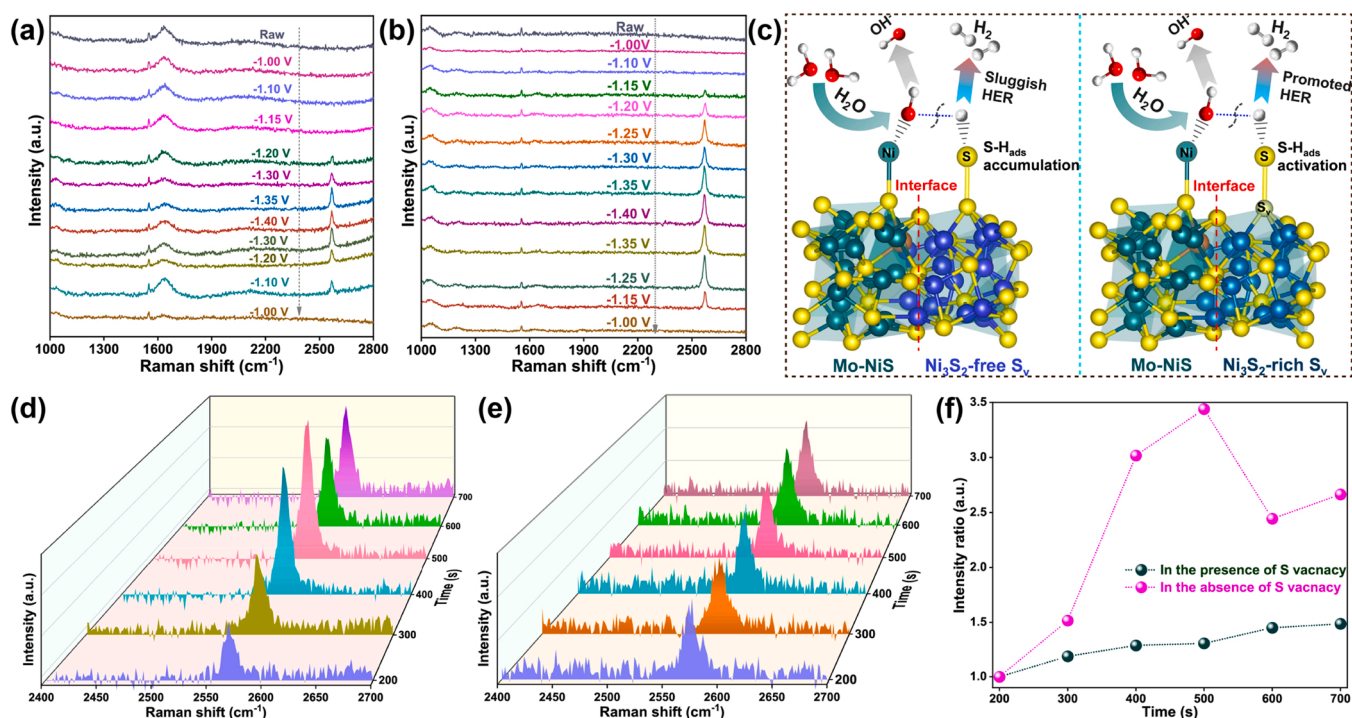


**Fig. 5.** In situ Raman spectra of the (a) Mo-NiS/Ni<sub>3</sub>S<sub>2</sub>-free S<sub>v</sub> and (b) rich S<sub>v</sub> electrocatalysts at various potentials versus Ag/AgCl for the alkaline HER process. (c) Schematic diagram illustrates the heterointerface and S-vacancy roles on the surface of the Mo-NiS/Ni<sub>3</sub>S<sub>2</sub>-free S<sub>v</sub> (left) and rich S<sub>v</sub> (right) electrocatalysts during the alkaline HER process. In situ Raman spectra of the (d) Mo-NiS/Ni<sub>3</sub>S<sub>2</sub>-free S<sub>v</sub> and (e) rich S<sub>v</sub> electrocatalysts as a function of time at an applied potential of -1.2 V versus Ag/AgCl in alkaline electrolytes. (f) S-H stretching vibration intensity ratio derived from in situ Raman spectra of the (d) Mo-NiS/Ni<sub>3</sub>S<sub>2</sub>-free S<sub>v</sub> and (e) rich S<sub>v</sub> electrocatalysts. (In Fig. 5(c) - Green ball: Ni atom on NiS side; Blue ball: Ni atom on Ni<sub>3</sub>S<sub>2</sub> side; yellow ball: S atom; brown ball: Mo atom).



decreasing to  $-1.40$  versus Ag/AgCl, the peak intensity of the S-H bond increased, suggesting the emergence of more S-H intermediates at the higher overpotential. After the introduction of S vacancies into Mo-NiS/Ni<sub>3</sub>S<sub>2</sub>-008S (Mo-NiS/Ni<sub>3</sub>S<sub>2</sub>-rich S<sub>v</sub>), a similar peak belonging to the S-H bond appeared at the lower potential of  $-1.15$  V versus Ag/AgCl and the peak intensity was sharply enhanced with the decrease of the applied potential. Notably, the intensity of the S-H bond in the presence of rich S<sub>v</sub> was clearly higher than that of free S<sub>v</sub>, suggesting that the rich S<sub>v</sub> was more favorable for the formation of S-H intermediates during the HER process (Fig. S27). When the potential was reversed, the peak intensity of the S-H bond decreased and finally disappeared at  $-1.0$  V versus Ag/AgCl, indicating that the S-H speciation formed on the surface of Mo-NiS/Ni<sub>3</sub>S<sub>2</sub>-rich S<sub>v</sub> was reversible. The broad characteristic peak located at  $1600\text{--}1700\text{ cm}^{-1}$  might be related to the impurities on the surface of the Mo-NiS/Ni<sub>3</sub>S<sub>2</sub>-free S<sub>v</sub> and it is difficult to assign the broad peak to a given reference. After the acidic etching, the surface impurities were removed and the corresponding peaks were disappeared, but no effect on the observation of S-H peaks. In addition, the weak peak of the S-H bond at  $2570\text{ cm}^{-1}$  was observed on the Ni<sub>3</sub>S<sub>2</sub> electrocatalysts,

while the peak signals of S-H speciation from the NiS electrocatalysts were invisible, suggesting that the Ni<sub>3</sub>S<sub>2</sub> are prone to adsorb H to form S-H species compared with the NiS (Fig. S28). From the above information, it was reasonably deduced that the S-H speciation on the Ni<sub>3</sub>S<sub>2</sub> of Mo-NiS/Ni<sub>3</sub>S<sub>2</sub>-rich S<sub>v</sub> surfaces was an important intermediate of the HER in our system.

Based on the Sabatier principle, in order to maximize the electrocatalytic activity, the binding of the reaction intermediates should be neither too strong nor too weak [44]. In this case, in situ Raman spectroscopy was re-employed to gain insight into the HER dynamics. As shown in Fig. 5d-f, in the absence of S vacancies, the peak intensity of S-H speciation on the surface was sharply increased as the time increased. In contrast, the peak signals of the S-H bond on the Mo-NiS/Ni<sub>3</sub>S<sub>2</sub>-rich S<sub>v</sub> surface varied more gradually over time. The enhanced peak intensity of the S-H species on the Mo-NiS/Ni<sub>3</sub>S<sub>2</sub>-free S<sub>v</sub> could be attributed to the strong binding of S-H intermediates, which resulted in the accumulation of S-H species, thereby poisoning the surface and slowing the HER kinetics. The S vacancies could weaken S-H bonds formed on Mo-NiS/Ni<sub>3</sub>S<sub>2</sub>-rich S<sub>v</sub> surfaces and optimize H desorption to

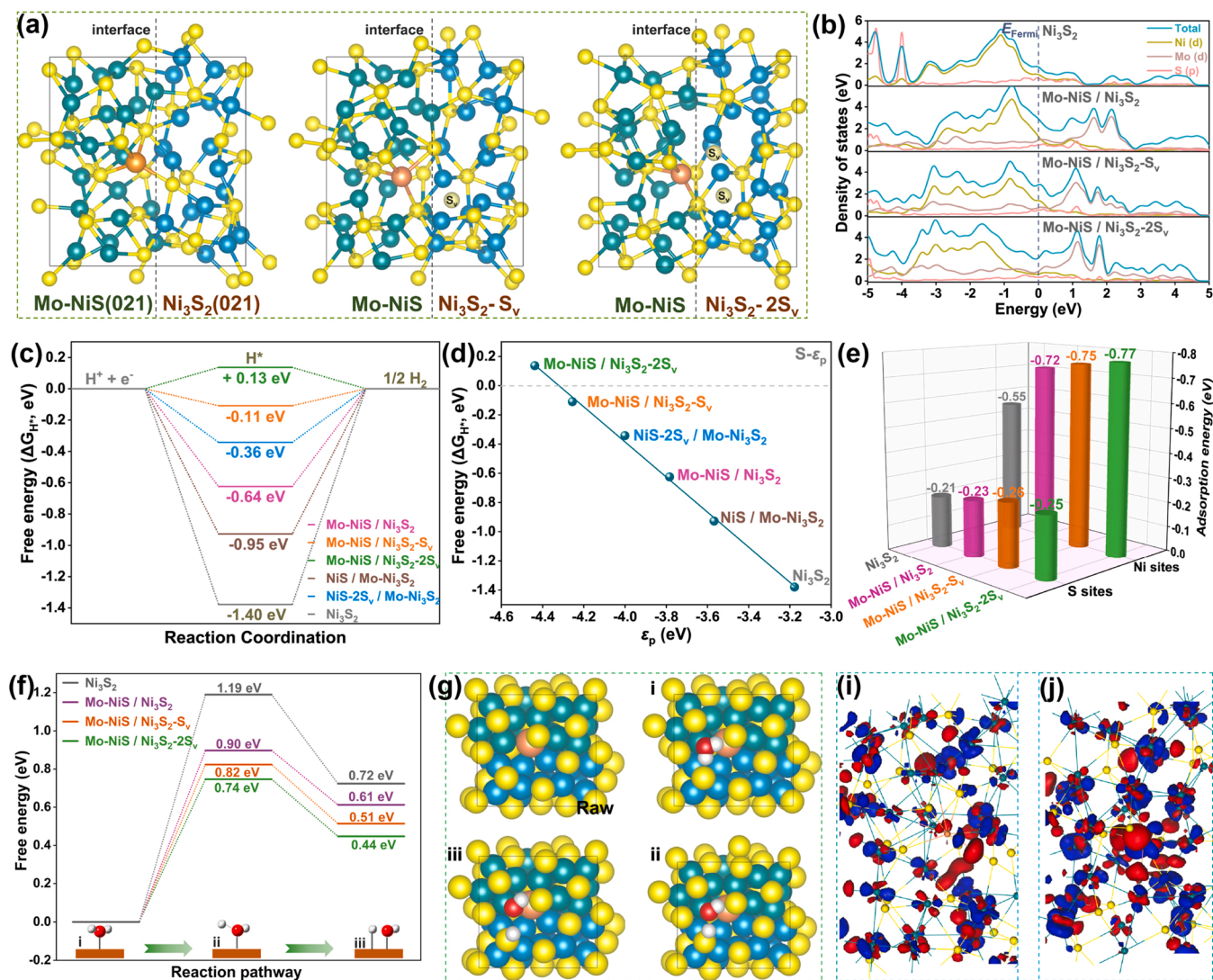


**Fig. 6.** (a) The top view of optimized calculation models of Mo-NiS (021)/Ni<sub>3</sub>S<sub>2</sub> (021), Mo-NiS (021)/Ni<sub>3</sub>S<sub>2</sub> (021)-S<sub>v</sub> and Mo-NiS (021)/Ni<sub>3</sub>S<sub>2</sub> (021)-2S<sub>v</sub>. (b) The electronic DOSs of the Ni<sub>3</sub>S<sub>2</sub>, Mo-NiS/Ni<sub>3</sub>S<sub>2</sub>, Mo-NiS/Ni<sub>3</sub>S<sub>2</sub>-S<sub>v</sub> and Mo-NiS/Ni<sub>3</sub>S<sub>2</sub>-2S<sub>v</sub> electrocatalysts. (c) HER free-energy diagram calculated for different catalysts. (d) Dependence of free energies of hydrogen adsorption on the p-band centers (ε<sub>p</sub>) of S-3p state. (e) Calculated water adsorption energy on both S and Ni sites and (f) reaction energy of water dissociation for the Ni<sub>3</sub>S<sub>2</sub>, Mo-NiS/Ni<sub>3</sub>S<sub>2</sub>, Mo-NiS/Ni<sub>3</sub>S<sub>2</sub>-S<sub>v</sub> and Mo-NiS/Ni<sub>3</sub>S<sub>2</sub>-2S<sub>v</sub> electrocatalysts. (g) Schematics of the water dissociation pathway on the Mo-NiS/Ni<sub>3</sub>S<sub>2</sub>-2S<sub>v</sub> electrocatalysts in alkaline electrolytes. The top view of charge density distribution calculated for the (i) Mo-NiS/Ni<sub>3</sub>S<sub>2</sub> and (j) Mo-NiS/Ni<sub>3</sub>S<sub>2</sub>-2S<sub>v</sub> electrocatalysts. (In Fig. 6a)- Green ball: Ni atom on NiS side; Blue ball: Ni atom on Ni<sub>3</sub>S<sub>2</sub> side; yellow ball: S atom; brown ball: Mo atom).

promote the Heyrovsky step of the HER, leading to high HER electrocatalytic activity. In short, the Mo-NiS/Ni<sub>3</sub>S<sub>2</sub>-rich S<sub>v</sub> featured an optimal interaction with atomic H and more favorable H desorption in alkaline HER compared to the Mo-NiS/Ni<sub>3</sub>S<sub>2</sub>-free S<sub>v</sub>, thus effectively accelerating the evolution kinetics of H<sub>ad</sub> to generate the H<sub>2</sub> (H<sub>ad</sub> + H<sub>2</sub>O + e<sup>-</sup> → H<sub>2</sub> + OH<sup>-</sup>) (Fig. 5c).

### 3.5. Theoretical calculation for HER

To further shed light on the origins of the superior HER activity of the Mo-NiS/Ni<sub>3</sub>S<sub>2</sub>-rich S<sub>v</sub>, theoretical simulations based on DFT calculations were performed. The structural models with various defects including heterointerfaces, doping and vacancies were firstly built and subjected to geometry optimization (Fig. 6a and S29). The formation energy of the Mo-NiS/Ni<sub>3</sub>S<sub>2</sub> was -0.244 eV, which was lower than that of the NiS/Mo-Ni<sub>3</sub>S<sub>2</sub> (-0.239 eV). This suggested that the Mo metal was likely to situate on the side of NiS. Further HR-TEM image in Fig. S30 indicated that Mo atoms concentrated more on the side of NiS, verifying the optimal Mo-NiS/Ni<sub>3</sub>S<sub>2</sub> structure. Compared with that of the NiS / Ni<sub>3</sub>S<sub>2</sub> ( $\Delta E = -0.235$  eV), the constructed Mo-NiS / Ni<sub>3</sub>S<sub>2</sub>-S<sub>v</sub> exhibited a lower formation energy of -0.246 eV. In contrast, the Mo-NiS / Ni<sub>3</sub>S<sub>2</sub> and Mo-NiS / Ni<sub>3</sub>S<sub>2</sub>-2S<sub>v</sub> presented identical values of -0.244 eV. Notably, the excess S vacancy may cause structural instability for the Mo-NiS / Ni<sub>3</sub>S<sub>2</sub>-3S<sub>v</sub> model due to the high energy of -0.219 eV. In addition, the calculated density of states (DOSs) for four models were continuous around the Fermi level, suggesting their intrinsic metallic characters (Fig. 6b). As is seen from the DOSs, the conductive characteristics of these electrocatalysts with heterointerfaces and S-vacancies are remarkably enhanced compared with the Ni<sub>3</sub>S<sub>2</sub>.

The free energy of adsorbing hydrogen intermediates ( $\Delta G_{H^*}$ ) is an important descriptor to characterize the HER activity, with an expected value close to zero, and was subsequently investigated on the model surface [45]. The  $\Delta G_{H^*}$  values on S adsorption sites of these model electrocatalysts were calculated based on the analytical results of in situ Raman spectroscopy (Fig. 6c and S31). For pure Ni<sub>3</sub>S<sub>2</sub>, the  $\Delta G_{H^*}$  value was deduced to be -1.40 eV, which was inert to the H<sub>2</sub> evolution. After the incorporation of Mo-NiS, the  $\Delta G_{H^*}$  value increased to -0.64 eV in the Mo-NiS / Ni<sub>3</sub>S<sub>2</sub> model. Importantly, the introduction of S<sub>v</sub> into the Ni<sub>3</sub>S<sub>2</sub> of the Mo-NiS / Ni<sub>3</sub>S<sub>2</sub> weakened the hydrogen desorption energy to -0.11 eV, which is close to -0.08 eV on the Pt (111) surface. Continuously increasing the S<sub>v</sub> concentration results in a slightly higher barrier energy of hydrogen adsorption with the positive value of 0.13 eV. Overall, it is proposed that the free S<sub>v</sub> in the Mo-NiS / Ni<sub>3</sub>S<sub>2</sub> model with a negative value of -0.64 eV represented low kinetics of hydrogen desorption, which would poison the catalyst surface, while the double-S<sub>v</sub> with a positive value of only 0.13 eV was beneficial for the kinetics of hydrogen adsorption/desorption, promoting the HER activity. The findings of the theoretical analysis are consistent with the experimental results from in situ Raman spectroscopy. In addition, the  $\Delta G_{H^*}$  values on the S sites from the NiS / Mo-Ni<sub>3</sub>S<sub>2</sub> and NiS-2S<sub>v</sub> / Mo-Ni<sub>3</sub>S<sub>2</sub> were also calculated to be -0.95 and -0.36 eV, respectively. The band centers of S-3p ( $\epsilon_p$ ) of these nickel sulfide electrocatalysts were computed from the partial density of states. The  $\epsilon_p$  value of the S-3p state was found to be some distance away from the  $E_{Fermi}$  after the introduction of defects and heterointerfaces into Ni<sub>3</sub>S<sub>2</sub> and assumed to be in the following order: Mo-NiS / Ni<sub>3</sub>S<sub>2</sub>-2S<sub>v</sub> (-4.44 eV) < Mo-NiS / Ni<sub>3</sub>S<sub>2</sub>-S<sub>v</sub> (-4.25 eV) < NiS-2S<sub>v</sub> / Mo-Ni<sub>3</sub>S<sub>2</sub> (-4.00 eV) < Mo-NiS / Ni<sub>3</sub>S<sub>2</sub> (-3.78 eV) < NiS / Mo-Ni<sub>3</sub>S<sub>2</sub> (-3.57 eV) < Ni<sub>3</sub>S<sub>2</sub> (-3.18 eV) (Fig. 6d). As expected, the comparison of  $\epsilon_p$  and  $\Delta G_{H^*}$  clearly demonstrated that the  $\epsilon_p$  has a negative linear correlation with  $\Delta G_{H^*}$  (Fig. 6d). The results are also in agreement with previous reports that  $\epsilon_p$  of the S-3p state can be regarded as an effective descriptor for H adsorption [16,46].

It is worth noting that in alkaline solution, the HER activity significantly depends on the dissociation ability of water via the Volmer step to provide a sufficient H source [47]. In order to answer the question of how to efficiently form the highly active species of S-H in the desired

model, DFT calculations were employed again. The formation of the S-H species is generally considered to involve three successive sub-steps, namely the adsorption, the activation, and the dissociation of H<sub>2</sub>O [48]. As shown in Fig. 6e and S32, compared with the S sites, the water molecules preferentially adsorb on the Ni atom of the NiS side with  $\Delta E$  (H<sub>2</sub>O) of -0.77 eV, -0.75 eV and -0.72 eV for the Mo-NiS / Ni<sub>3</sub>S<sub>2</sub>-2S<sub>v</sub>, Mo-NiS / Ni<sub>3</sub>S<sub>2</sub>-S<sub>v</sub>, and Mo-NiS / Ni<sub>3</sub>S<sub>2</sub>, respectively, which were lower than that of Ni<sub>3</sub>S<sub>2</sub> (-0.55 eV). More importantly, the nickel sulfide polymorph also presented lower energy barriers ( $\Delta G_B = 0.90$  eV) for the cleavage of H<sub>2</sub>O into \*OH and \*H compared with the Ni<sub>3</sub>S<sub>2</sub> ( $\Delta G_B = 1.19$  eV), highlighting the critical role of the heterointerfaces for H<sub>2</sub>O dissociation in the Volmer step (Fig. 6f and S33). Notably, the Mo-NiS/Ni<sub>3</sub>S<sub>2</sub>-2S<sub>v</sub> exhibited the lowest H<sub>2</sub>O adsorption and dissociation energy ( $\Delta G_B = 0.74$  eV) (Figs. 6e and 6f). It was reasonably believed that the HO-H bond cleavage of H<sub>2</sub>O on Ni centers of the Mo-NiS side would result in the OH being retained on Ni atoms, while H atoms could cross the heterointerfaces to transfer to nearby S atoms of Ni<sub>3</sub>S<sub>2</sub> side followed by hydrogen evolution (Fig. 6g). As a result, the heterointerfaces of nickel sulfide polymorphs could promote water dissociation and the rich S<sub>v</sub> on the Ni<sub>3</sub>S<sub>2</sub> sides are responsible for the activation of hydrogen intermediates (S-H), which synergistically enhance the HER activity of the Mo-NiS/Ni<sub>3</sub>S<sub>2</sub>-2S<sub>v</sub> (Fig. 5c). More importantly, for the nickel sulfide polymorphs, it is theoretically possible that their heterointerfaces and rich S<sub>v</sub> could present the cooperativity to facilitate water dissociation and evolution of H intermediates to H<sub>2</sub>. In addition, a significant electron redistribution in the Mo-NiS/Ni<sub>3</sub>S<sub>2</sub>-2S<sub>v</sub> crystals has been induced by defects and heterointerfaces. The red section is related to the electron accumulation, while the blue section means electron deficiency. As shown in Fig. 6i-j and S34, Supporting Information, we observed that a strong charge redistribution occurred at the interface region of three heterostructured models. Furthermore, a slightly higher electron density around the S atom at the Mo-NiS/Ni<sub>3</sub>S<sub>2</sub>-2S<sub>v</sub> interface, relative to the Mo-NiS/Ni<sub>3</sub>S<sub>2</sub> interface, suggested that S<sub>v</sub> was favorable for boosting the interface electronic interaction between Mo-NiS and Ni<sub>3</sub>S<sub>2</sub>-2S<sub>v</sub>. This electron redistribution could play an important role in strengthening the conductivity of the electrocatalyst and manipulating HER kinetics. In summary, the moderate  $\Delta G_{H^*}$  and low  $\Delta G_B$ , as well as high conductivity, in the Mo-NiS/Ni<sub>3</sub>S<sub>2</sub>-rich S<sub>v</sub> catalysts led to a remarkably enhanced HER activity as obtained experimentally.

## 4. Conclusions

In this study, heterointerfaces and S<sub>v</sub> were successfully introduced into Ni<sub>3</sub>S<sub>2</sub> to construct the Mo-NiS/Ni<sub>3</sub>S<sub>2</sub>-rich S<sub>v</sub> electrocatalyst via a hydrothermal sulfurization-acid assisted etching method. The heterointerface structure formed between NiS and Ni<sub>3</sub>S<sub>2</sub> components was closely associated with the additive amount. The Mo-NiS/Ni<sub>3</sub>S<sub>2</sub>-rich S<sub>v</sub> electrocatalyst exhibited an excellent HER activity and stability in alkaline solutions. In situ Raman analysis and theoretical simulation revealed that the superior alkaline HER could be attributed to the cooperative action of heterostructures and rich S<sub>v</sub>, where the Ni atoms in the Mo-NiS components were the reaction sites for promoting water dissociation, favoring the hydrogen transfer to nearby S atoms of Ni<sub>3</sub>S<sub>2</sub>, while the rich S<sub>v</sub> can expedite the evolution of H<sup>+</sup> to H<sub>2</sub> with a low  $|\Delta G_{H^*}|$  value. These findings of this study not only deepen the fundamental understanding of the heterostructures and vacancies in promoting water destabilization and balancing the hydrogen-binding energy, but also provide valuable guidance in the development of advanced electrocatalysts for alkaline HER.

### CRedit authorship contribution statement

**Kai Zhang:** Conceptualization, Methodology, Formal analysis, Investigation, Visualization, Funding acquisition, Writing – original draft. **Yuanxiao Duan:** Investigation, Methodology, Formal analysis. **Nigel Graham:** Supervision, Writing – review & editing. **Wenzheng Yu:**



Conceptualization, Supervision, Funding acquisition, Writing – review & editing.

## Declaration of Competing Interest

The authors declare that they have no known competing financial interests or personal relationships that could have appeared to influence the work reported in this paper.

## Data Availability

Data will be made available on request.

## Acknowledgment

This work was financially supported by the National Natural Science Foundation of China (Grants 52000178), and Key Research and Development Plan of the Ministry of Science and Technology (2019YFD1100104 and 2019YFC1906501). It was also supported by Open Project of State Key Laboratory of Urban Water Resource and Environment, Harbin Institute of Technology (No. HC202158).

## Appendix A. Supporting information

Supplementary data associated with this article can be found in the online version at [doi:10.1016/j.apcatb.2022.122144](https://doi.org/10.1016/j.apcatb.2022.122144).

## References

- [1] Y. Wang, X. Li, M. Zhang, J. Zhang, Z. Chen, X. Zheng, Z. Tian, N. Zhao, X. Han, K. Zaghib, Y. Wang, Y. Deng, W. Hu, Highly active and durable single-atom tungsten-doped  $\text{Ni}_{0.5}\text{Se}_{0.5}$  nanosheet @  $\text{Ni}_{0.5}\text{Se}_{0.5}$  nanorod heterostructures for water splitting, *Adv. Mater.* 34 (2022) 2107053, <https://doi.org/10.1002/adma.202107053>.
- [2] T. Wang, L. Tao, X. Zhu, C. Chen, W. Chen, S. Du, Y. Zhou, B. Zhou, D. Wang, C. Xie, P. Long, W. Li, Y. Wang, R. Chen, Y. Zou, X.Z. Fu, Y. Li, X. Duan, S. Wang, Combined anodic and cathodic hydrogen production from aldehyde oxidation and hydrogen evolution reaction, *Nat. Catal.* 5 (2021) 66–73, <https://doi.org/10.1038/s41929-021-00721-y>.
- [3] W. Zhong, B. Xiao, Z. Lin, Z. Wang, L. Huang, S. Shen, Q. Zhang, L. Gu,  $\text{RhSe}_2$ : a superior 3D electrocatalyst with multiple active facets for hydrogen evolution reaction in both acid and alkaline solutions, *Adv. Mater.* 33 (2021) 2007894, <https://doi.org/10.1002/adma.202007894>.
- [4] Z. Chen, Y. Xu, D. Ding, G. Song, X. Gan, H. Li, W. Wei, J. Chen, Z. Li, Z. Gong, X. Dong, C. Zhu, N. Yang, J. Ma, R. Gao, D. Luo, S. Cong, L. Wang, Z. Zhao, Y. Cui, Thermal migration towards constructing W-W dual-sites for boosted alkaline hydrogen evolution reaction, *Nat. Commun.* 13 (2022) 763, <https://doi.org/10.1038/s41467-022-28413-6>.
- [5] J. Li, Y. Li, J. Wang, C. Zhang, H. Ma, C. Zhu, D. Fan, Z. Guo, M. Xu, Y. Wang, H. Ma, Elucidating the critical role of ruthenium single atom sites in water dissociation and dehydrogenation behaviors for robust hydrazine oxidation-boosted alkaline hydrogen evolution, *Adv. Funct. Mater.* 32 (2022) 2109439, <https://doi.org/10.1002/adfm.202109439>.
- [6] X. Han, X. Wu, Y. Deng, J. Liu, J. Lu, C. Zhong, W. Hu, Ultrafine Pt nanoparticle-decorated pyrite-type  $\text{CoS}_2$  nanosheet arrays coated on carbon cloth as a bifunctional electrode for overall water splitting, *Adv. Energy Mater.* 8 (2018) 1800935, <https://doi.org/10.1002/aenm.201800935>.
- [7] H. Jin, X. Liu, Y. Jiao, A. Vasileff, Y. Zheng, S.Z. Qiao, Constructing tunable dual active sites on two-dimensional  $\text{C}_3\text{N}_4$ @ $\text{MoN}$  hybrid for electrocatalytic hydrogen evolution, *Nano Energy* 53 (2018) 690–697, <https://doi.org/10.1016/j.nanoen.2018.09.046>.
- [8] Y. Wang, X. Li, M. Zhang, Y. Zhou, D. Rao, C. Zhong, J. Zhang, X. Han, W. Hu, Y. Zhang, K. Zaghib, Y. Wang, Y. Deng, Lattice-strain engineering of homogeneous  $\text{Ni}_{0.5}\text{Se}_{0.5}$  core-shell nanostructure as a highly efficient and robust electrocatalyst for overall water splitting, *Adv. Mater.* 32 (2020) 2000231, <https://doi.org/10.1002/adma.202000231>.
- [9] K. Zhang, C. Liu, N. Graham, G. Zhang, W. Yu, Modulation of dual centers on cobalt-molybdenum oxides featuring synergistic effect of intermediate activation and radical mediator for electrocatalytic urea splitting, *Nano Energy* 87 (2021), 106217, <https://doi.org/10.1016/j.nanoen.2021.106217>.
- [10] J.Y. Xue, F.L. Li, B. Chen, H. Geng, W. Zhang, W.-Y. Xu, H. Gu, P. Braunstein, J. P. Lang, Engineering multiphase  $\text{MoSe}_2$ /NiSe heterostructure interfaces for superior hydrogen production electrocatalysis, *Appl. Catal. B Environ.* 312 (2022), 121434, <https://doi.org/10.1016/j.apcatb.2022.121434>.
- [11] Y. Zhang, Y. Lin, T. Duan, L. Song, Interfacial engineering of heterogeneous catalysts for electrocatalysis, *Mater. Today* 48 (2021) 115–134, <https://doi.org/10.1016/j.mattod.2021.02.004>.
- [12] Q. Xu, J. Zhang, H. Zhang, L. Zhang, L. Chen, Y. Hu, H. Jiang, C. Li, Atomic heterointerface engineering overcomes the activity limitation of electrocatalysts and promises highly-efficient alkaline water splitting, *Energy Environ. Sci.* 14 (2021) 5228–5259, <https://doi.org/10.1039/D1EE02105B>.
- [13] P. Wang, X. Zhang, J. Zhang, S. Wan, S. Guo, G. Lu, J. Yao, X. Huang, Precise tuning in platinum-nickel/nickel sulfide interface nanowires for synergistic hydrogen evolution catalysis, *Nat. Commun.* 8 (2017) 14580, <https://doi.org/10.1038/ncomms14580>.
- [14] T. Liu, A. Li, C. Wang, W. Zhou, S. Liu, L. Guo, Interfacial electron transfer of  $\text{Ni}_2\text{P}$ - $\text{NiP}_2$  polymorphs inducing enhanced electrochemical properties, *Adv. Mater.* 30 (2018) 1803590, <https://doi.org/10.1002/adma.201803590>.
- [15] K. Zhang, G. Zhang, Q.H. Ji, J.H. Qu, H.J. Liu, Arrayed cobalt phosphide electrocatalyst achieves low energy consumption and persistent  $\text{H}_2$  liberation from anodic chemical conversion, *Nano Micro Lett.* 12 (2020) 154, <https://doi.org/10.1007/s40820-020-00486-2>.
- [16] J. Wu, Q. Zhang, K. Shen, R. Zhao, W. Zhong, C. Yang, H. Xiang, X. Li, N. Yang, Modulating interband energy separation of boron-doped  $\text{Fe}_7\text{S}_8/\text{FeS}_2$  electrocatalysts to boost alkaline hydrogen evolution reaction, *Adv. Funct. Mater.* 32 (2021) 2107802, <https://doi.org/10.1002/adfm.202107802>.
- [17] L. Tan, J. Yu, H. Wang, H. Gao, X. Liu, L. Wang, X. She, T. Zhan, Controllable synthesis and phase-dependent catalytic performance of dual-phase nickel selenides on Ni foam for overall water splitting, *Appl. Catal. B Environ.* 303 (2022), 120915, <https://doi.org/10.1016/j.apcatb.2021.120915>.
- [18] Z. Wang, S. Wang, L. Ma, Y. Guo, J. Sun, N. Zhang, R. Jiang, Water-induced formation of  $\text{Ni}_2\text{P}$ - $\text{Ni}_{12}\text{P}_5$  interfaces with superior electrocatalytic activity toward hydrogen evolution reaction, *Small* 17 (2021) 2006770, <https://doi.org/10.1002/smll.202006770>.
- [19] W. Liu, X. Wang, F. Wang, K. Du, Z. Zhang, Y. Guo, H. Yin, D. Wang, A durable and pH-universal self-standing  $\text{MoC-Mo}_2\text{C}$  heterojunction electrode for efficient hydrogen evolution reaction, *Nat. Commun.* 12 (2021) 6776, <https://doi.org/10.1038/s41467-021-27118-6>.
- [20] S. Jiao, X. Fu, S. Wang, Y. Zhao, Perfecting electrocatalysts via imperfections: towards the large-scale deployment of water electrolysis technology, *Energy Environ. Sci.* 14 (2021) 1722–1770, <https://doi.org/10.1039/D0EE03635H>.
- [21] X. Wang, Y. Zhang, H. Si, Q. Zhang, J. Wu, L. Gao, X. Wei, Y. Sun, Q. Liao, Z. Zhang, K. Ammarah, L. Gu, Z. Kang, Y. Zhang, Single-atom vacancy defect to trigger high-efficiency hydrogen evolution of  $\text{MoS}_2$ , *J. Am. Chem. Soc.* 142 (2020) 4298–4308, <https://doi.org/10.1021/jacs.9b12113>.
- [22] P. Wang, T. Wang, R. Qin, Z. Pu, C. Zhang, J. Zhu, D. Chen, D. Feng, Z. Kou, S. Mu, J. Wang, Swapping catalytic active sites from cationic Ni to anionic S in nickel sulfide enables more efficient alkaline hydrogen generation, *Adv. Energy Mater.* 12 (2022) 2103359, <https://doi.org/10.1002/aenm.202103359>.
- [23] Y. Sun, J. Wu, Z. Zhang, Q. Liao, S. Zhang, X. Wang, Y. Xie, K. Ma, Z. Kang, Y. Zhang, Phase reconfiguration of multivalent nickel sulfides in hydrogen evolution, *Energy Environ. Sci.* 15 (2022) 633–644, <https://doi.org/10.1039/D1EE02985A>.
- [24] J.X. Feng, J.Q. Wu, Y.X. Tong, G.R. Li, Efficient hydrogen evolution on Cu nanodots-decorated  $\text{Ni}_3\text{S}_2$  nanotubes by optimizing atomic hydrogen adsorption and desorption, *J. Am. Chem. Soc.* 140 (2018) 610–617, <https://doi.org/10.1021/jacs.7b08521>.
- [25] X. Zhao, J. Feng, J. Liu, W. Shi, G. Yang, G.C. Wang, P. Cheng, An efficient, visible-light-driven, hydrogen evolution catalyst  $\text{NiS}/\text{Zn}_x\text{Cd}_{1-x}\text{S}$  nanocrystal derived from a metal-organic framework, *Angew. Chem. Int. Ed.* 57 (2018) 9790–9794, <https://doi.org/10.1002/anie.201805425>.
- [26] C. Zhang, Y. Shi, Y. Yu, Y. Du, B. Zhang, Engineering sulfur defects, atomic thickness, and porous structures into cobalt sulfide nanosheets for efficient electrocatalytic alkaline hydrogen evolution, *ACS Catal.* 8 (2018) 8077–8083, <https://doi.org/10.1021/acscatal.8b02056>.
- [27] M.D. Segall, P.J.D. Lindan, M.J. Probert, C.J. Pickard, P.J. Hasnip, et al., First-principles simulation: ideas, illustrations and the CASTEP code, *J. Phys.: Condens. Matter* 14 (2002) 2717, <https://doi.org/10.1088/0953-8984/14/11/301>.
- [28] J.P. Perdew, K. Burke, M. Ernzerhof, Generalized gradient approximation made simple, *Phys. Rev. Lett.* 77 (1996) 3865, <https://doi.org/10.1103/PhysRevLett.77.3865>.
- [29] Z. Wang, J. Chen, E. Song, N. Wang, J. Dong, X. Zhang, P.M. Ajayan, W. Yao, C. Wang, J. Liu, J. Shen, M. Ye, Manipulation on active electronic states of metastable phase  $\beta\text{-NiMoO}_4$  for large current density hydrogen evolution, *Nat. Commun.* 12 (2021) 5960, <https://doi.org/10.1038/s41467-021-26256-1>.
- [30] P. Luo, H. Zhang, L. Liu, Y. Zhang, J. Deng, C. Xu, N. Hu, Y. Wang, Targeted synthesis of unique nickel sulfide ( $\text{NiS}$ ,  $\text{NiS}_2$ ) microarchitectures and the applications for the enhanced water splitting system, *ACS Appl. Mater. Interfaces* 9 (2017) 2500–2508, <https://doi.org/10.1021/acsami.6b13984>.
- [31] G. Zhang, Y.S. Feng, W.T. Lu, D. He, C.Y. Wang, Y.K. Li, X.Y. Wang, F.F. Cao, Enhanced catalysis of electrochemical overall water splitting in alkaline media by Fe doping in  $\text{Ni}_3\text{S}_2$  nanosheet arrays, *ACS Catal.* 8 (2018) 5431–5441, <https://doi.org/10.1021/acscatal.8b00413>.
- [32] C. Dai, B. Li, J. Li, B. Zhao, R. Wu, H. Ma, X. Duan, Controllable synthesis of  $\text{NiS}$  and  $\text{NiS}_2$  nanoplates by chemical vapor deposition, *Nano Res* 13 (2020) 2506–2511, <https://doi.org/10.1007/s12274-020-2887-5>.
- [33] Z. Wang, S. Shen, Z. Lin, W. Tao, Q. Zhang, F. Meng, L. Gu, W. Zhong, Regulating the local spin state and band structure in  $\text{Ni}_3\text{S}_2$  nanosheet for improved oxygen evolution activity, *Adv. Funct. Mater.* (2022) 2112832, <https://doi.org/10.1002/adfm.202112832>.
- [34] Z. Zhai, C. Li, L. Zhang, H.C. Wu, L. Zhang, N. Tang, W. Wang, J. Gong, Dimensional construction and morphological tuning of heterogeneous  $\text{MoS}_2/\text{NiS}$

- electrocatalysts for efficient overall water splitting, *J. Mater. Chem. A* 6 (2018) 9833–9838, <https://doi.org/10.1039/C8TA03304H>.
- [35] C. Yang, M.Y. Gao, Q.B. Zhang, J.R. Zeng, X.T. Li, A.P. Abbott, In-situ activation of self-supported 3D hierarchically porous  $\text{Ni}_3\text{S}_2$  films grown on nanoporous copper as excellent pH-universal electrocatalysts for hydrogen evolution reaction, *Nano Energy* 36 (2017) 85–94, <https://doi.org/10.1016/j.nanoen.2017.04.032>.
- [36] R. Zheng, C. Shu, X. Chen, Y. Yan, M. He, D. Du, L. Ren, A. Hu, J. Long, Unique intermediate adsorption enabled by anion vacancies in metal sulfide embedded MXene nanosheets overcoming kinetic barriers of oxygen electrode reactions in lithium-oxygen batteries, *Energy Storage Mater.* 40 (2021) 41–50, <https://doi.org/10.1016/j.ensm.2021.04.041>.
- [37] K. Lu, F. Xia, B. Li, Y. Liu, I.B. Abdul Razak, S. Gao, J. Kaelin, D.E. Brown, Y. Cheng, Synergistic multisites  $\text{Fe}_2\text{Mo}_6\text{S}_8$  electrocatalysts for ambient nitrogen conversion to ammonia, *ACS Nano* 15 (2021) 16887–16895, <https://doi.org/10.1021/acsnano.1c07771>.
- [38] T. Ouyang, Y.Q. Ye, C.Y. Wu, K. Xiao, Z.Q. Liu, Heterostructures composed of N-doped carbon nanotubes encapsulating cobalt and beta- $\text{Mo}_2\text{C}$  nanoparticles as bifunctional electrodes for water splitting, *Angew. Chem. Int. Ed.* 58 (2019) 4923–4928, <https://doi.org/10.1002/anie.201814262>.
- [39] S. Zhang, Q. Zhou, Z. Shen, X. Jin, Y. Zhang, M. Shi, J. Zhou, J. Liu, Z. Lu, Y. N. Zhou, H. Zhang, Sulfophobic and vacancy design enables self-cleaning electrodes for efficient desulfurization and concurrent hydrogen evolution with low energy consumption, *Adv. Funct. Mater.* 31 (2021) 2101922, <https://doi.org/10.1002/adfm.202101922>.
- [40] C. Yang, R. Zhao, H. Xiang, J. Wu, W. Zhong, X. Li, Q. Zhang, Structural transformation of molybdenum carbide with extensive active centers for superior hydrogen evolution, *Nano Energy* 98 (2022), 107232, <https://doi.org/10.1016/j.nanoen.2022.107232>.
- [41] J. Ji, Q. Yan, P. Yin, S. Mine, M. Matsuoka, M. Xing, Defects on  $\text{CoS}_{2-x}$ : tuning redox reactions for sustainable degradation of organic pollutants, *Angew. Chem. Int. Ed.* 60 (2021) 2903–2908, <https://doi.org/10.1002/anie.202013015>.
- [42] J. Zhang, Z. Zhang, Y. Ji, J. Yang, K. Fan, X. Ma, C. Wang, R. Shu, Y. Chen, Surface engineering induced hierarchical porous  $\text{Ni}_{12}\text{P}_5\text{-Ni}_2\text{P}$  polymorphs catalyst for efficient wide pH hydrogen production, *Appl. Catal. B Environ.* 282 (2021), 119609, <https://doi.org/10.1016/j.apcatb.2020.119609>.
- [43] S. Guo, Y. Li, S. Tang, Y. Zhang, X. Li, A.J. Sobrido, M.M. Titirici, B. Wei, Monitoring hydrogen evolution reaction intermediates of transition metal dichalcogenides via operando raman spectroscopy, *Adv. Funct. Mater.* 30 (2020) 2003035, <https://doi.org/10.1002/adfm.202003035>.
- [44] H. Tian, Y. He, Q. Zhao, J. Li, X. Shao, Z. Zhang, X. Huang, C. Lu, K. Wang, Q. Jiang, A.M.C. Ng, H. Xu, S.Y. Tong, Avoiding Sabatier's conflict in bifunctional heterogeneous catalysts for the WGS reaction, *Chem* 7 (2021) 1271–1283, <https://doi.org/10.1016/j.chempr.2021.01.018>.
- [45] H. Jiang, L. Yan, S. Zhang, Y. Zhao, X. Yang, Y. Wang, J. Shen, X. Zhao, L. Wang, Electrochemical surface restructuring of phosphorus-doped carbon@MoP electrocatalysts for hydrogen evolution, *Nano Micro Lett.* 13 (2021) 215, <https://doi.org/10.1007/s40820-021-00737-w>.
- [46] J. Wang, Z. Zhang, H. Song, B. Zhang, J. Liu, X. Shai, L. Miao, Water dissociation kinetic-oriented design of nickel sulfides via tailored dual sites for efficient alkaline hydrogen evolution, *Adv. Funct. Mater.* 31 (2020) 2008578, <https://doi.org/10.1002/adfm.202008578>.
- [47] Y.N. Zhou, F.L. Wang, J. Nan, B. Dong, H.Y. Zhao, F.G. Wang, N. Yu, R.N. Luan, D. P. Liu, Y.M. Chai, High-density ultrafine  $\text{RuP}_2$  with strong catalyst-support interaction driven by dual-ligand and tungsten-oxygen sites for hydrogen evolution at  $1\text{ A cm}^{-2}$ , *Appl. Catal. B Environ.* 304 (2022), 120917, <https://doi.org/10.1016/j.apcatb.2021.120917>.
- [48] C. Yang, W. Zhong, K. Shen, Q. Zhang, R. Zhao, H. Xiang, J. Wu, X. Li, N. Yang, Electrochemically reconstructed  $\text{Cu-FeOOH/Fe}_3\text{O}_4$  catalyst for efficient hydrogen evolution in alkaline media, *Adv. Energy Mater.* 12 (2022) 2200077, <https://doi.org/10.1002/aenm.202200077>.